

ORGANIZATION COVER PAGE

**FINAL REPORT
to the
UNITED STATES OFFICE OF NAVAL RESEARCH**

**New Magnetic Materials and Phenomena for Radar
and Microwave Signal Processing Devices -
Bulk and Thin Film Ferrites and Metallic Films**

**ONR N00014-07-1-0597, 02 February 2007 - 30 September
2008**

Carl E. Patton, Principal Investigator
Department of Physics
Colorado State University
Fort Collins, Colorado 80523

Date of Report:
15 February 2009

Contact Information
Telephone: (970) 491-5083
FAX: (970) 491-7947
E-MAIL: patton@lamar.colostate.edu

20090220315

| | | | | |
|---|---|--|---|--|
| REPORT DOCUMENTATION PAGE | | | Form Approved OMB No. 0704-0188 | |
| Public reporting burden for this collection of information is estimated to average 1 hour per response, including the time for reviewing instructions, searching existing data sources, gathering and maintaining the data needed, and completing and reviewing the collection of information. Send comments regarding this burden estimate or any other aspect of this collection of information, including suggestions for reducing this burden, to Washington Headquarters Services, Directorate for Information Operations and Reports, 1215 Jefferson Davis Highway, Suite 1204, Arlington, VA 22202-4302, and to the Office of Management and Budget, Paperwork Reduction Project (0704-0188), Washington, DC 20503. | | | | |
| 1. AGENCY USE ONLY (Leave blank) | | 2. REPORT DATE 15 FEBRUARY 2009 | 3. REPORT TYPE AND DATES COVERED FINAL REPORT, 02 FEBRUARY 2007 - 30 SEPTEMBER 2008 | |
| 4. TITLE AND SUBTITLE New magnetic materials and phenomena for radar and microwave signal processing devices - bulk and thin film ferrites and metallic films | | | 5. FUNDING NUMBERS N00014-07-1-0597 | |
| 6. AUTHOR(S) Carl E. Patton | | | | |
| 7. Performing organization name(s) and address(es) Department of Physics Colorado State University Fort Collins, CO 80523-1875 | | | 8. PERFORMING ORGANIZATION REPORT NUMBER None | |
| 9. SPONSORING/MONITORING AGENCY NAME(S) AND ADDRESS(ES) Office of Naval Research (ONR) 875 North Randolph Street Arlington, VA 22203-1995 | | | 10. SPONSORING/MONITORING AGENCY REPORT NUMBER None | |
| II. SUPPLEMENTARY NOTES The view, opinions and/or findings contained in this report are those of the author(s) and should not be construed as an official Office of Naval Research position, policy, or decision, unless so designated by other documentation. | | | | |
| 12a. DISTRIBUTION/AVAILABILITY STATEMENT Approved for public release; distribution unlimited. | | | 12b. DISTRIBUTION CODE | |
| 13. ABSTRACT (Maximum 200 words) ONR Grant ONR N00014-07-1-0597 has supported a four phase program. Under Phase (1), there were three materials thrusts, (a) hybrid pulse laser deposited and liquid phase epitaxy films of low loss cubic yttrium iron garnet (YIG) and uniaxial barium hexaferrite, (b) bulk and thick film ultra-dense fine grain polycrystalline YIG materials, and (c) high magnetization metallic films, notably of Permalloy, iron, and FeTiN. Under Phase (2), the focus was on magnetic loss properties, both on and away from the peak in the ferromagnetic resonance (FMR) response, and the change in the microwave response at high power. Under Phase (3), the Magnetism Laboratory at Colorado State University (CSU) worked with other colleagues and collaborators in sister ONR programs to combine the magnetic systems developed and characterized at CSU with ferroelectric films and systems to achieve new multifunctional properties. Under Phase (4), the unique expertise of the CSU facility in Brillouin light scattering was applied to ferrite film systems, among others, to study the basic linear and nonlinear magnetic excitation properties in delay line structures. (173 words) | | | | |
| 14. SUBJECT TERMS Microwave ferrites, yttrium iron garnet, hexagonal ferrites, polycrystalline ferrites, single crystal ferrites, thin films, ferromagnetic resonance, ferromagnetic resonance linewidth, effective linewidth, spin wave instability, spin wave linewidth, metal alloy films, magneto-optic Kerr effect, Suhl processes, barium ferrite, barium strontium titanate, multiferroic heterostructures. | | | 15. NUMBER OF PAGES 37 (including this form) | |
| | | | 16. PRICE CODE | |
| 17. SECURITY CLASSIFICATION OF REPORT Unclassified | 18. SECURITY CLASSIFICATION OF THIS PAGE Unclassified | 19. SECURITY CLASSIFICATION OF ABSTRACT Unclassified | 20. LIMITATION OF ABSTRACT UL | |

A. TABLE OF CONTENTS

| | |
|--|--------|
| ORGANIZATION COVER PAGE | 1 |
| A. TABLE OF CONTENTS..... | 2 |
| B. ABSTRACT..... | 2 |
| C. RESULTS..... | 3 |
| 1. Overview | 3 |
| 2. Education and Human Resources | 4 |
| 3. Publication list..... | 4 |
| Publications | 5 - 36 |

B. ABSTRACT

ONR Grant ONR N00014-07-1-0597 has supported a four phase program. Under Phase (1), there were three materials thrusts. (a) The first was on the continued development of hybrid pulse laser deposited and liquid phase epitaxy films of low loss cubic yttrium iron garnet (YIG) and lithium ferrite, uniaxial barium hexaferrite, and planar zinc-Y hexaferrite. (b) The second was on a renewed effort on bulk and thick film ultra-dense fine grain polycrystalline YIG and spinel ferrite materials, and on native oxide multilayers. (c) The third was on high magnetization metallic films, notably of Permalloy, iron, and FeTiN. All of these classes of materials hold promise for different defense related radar and signal processing device applications. The ultimate applications include high Q filters, phase locked microwave pulse sources, microwave and millimeter wave devices such as isolators, circulators, phase shifters, secure signal processing devices, and wide band tunable filters. Under Phase (2), the focus was on magnetic loss properties, both on and away from the peak in the ferromagnetic resonance (FMR) response, and the change in the microwave response at high power. These studies are important because the low power losses control device insertion loss, while the high power response sets the limit on input power. These properties control the viability of a given material for useful devices. Under Phase (3), the Magnetism Laboratory at Colorado State University (CSU) worked with other colleagues and collaborators in sister ONR programs at the University of California - Berkeley, Georgia Institute of Technology, and Oakland University to combine the magnetic systems developed and characterized at CSU with ferroelectric films and systems to achieve new multifunctional properties. Under Phase (4), the unique expertise of the CSU facility in Brillouin light scattering was applied to the BiFeO₃ system, among others, to study the basic magnetic excitation properties of these new and exciting multi-ferroic systems that exhibit both ferroelectricity and canted ferrimagnetic, or weak ferromagnetic, order. One can envision the use of electric fields to tune the spin wave response in this system and produce a new class of low power consumption tunable microwave and millimeter wave devices.

C. RESULTS

1. Overview

There are few centers of expertise in the world which are capable of quality research and development work in the area of microwave magnetic materials. The Magnetism Laboratory in the Department of Physics at Colorado State University (CSU), Fort Collins, is well equipped for a wide range of high frequency magnetic measurements at low and high power, at low and high field, over a wide range of frequencies, and as a function of temperature. This team also has the resident expertise to select and investigate the critical materials problems that are relevant to the needs cited above. Much of this infrastructure has been established over the past decade with Office of Naval Research (ONR) support.

Past CSU work has addressed and solved numerous microwave loss and materials problems as they relate to both fundamental understanding and device needs. In the area of ferrites, these include (1) the role of microstructure in the low and high power loss properties of polycrystalline yttrium iron garnet (YIG), (2) the low and high power microwave properties of substituted lithium ferrite materials, (3) the microwave properties of arc plasma spray lithium ferrite, (4) the origins of the large losses in hexagonal ferrite materials for millimeter wave applications, (5) the high power microwave properties of hexagonal ferrite materials, (6) the characterization of liquid phase epitaxy yttrium iron garnet (YIG) films produced with special fluxes, (7) the characterization of ultra dense polycrystalline ferrites for microwave applications prepared by hot isostatic pressing (HIPING) techniques, (8) the growth and characterization of pulsed laser deposited (PLD) ferrite films of YIG and barium hexaferrite with losses which are as good as the best bulk single crystals, and (9) the successful PLD growth of low loss zinc lithium ferrite films.

In the area of metallic ferromagnetic films, which represents a promising system for wide band tunable filters in the microwave and millimeter regime, for example, CSU has been a key contributor to (1) the understanding of phenomenological damping in metal films, (2) the elucidation of microwave loss properties and most recently, (3) a new understanding of the high power properties as well. A significant part of this work has been accomplished during the past and current grant periods under ONR support.

In addition to the above microwave/millimeter wave materials characterization and device physics development work, the Colorado State University program has provided numerous contributions that have advanced the understanding of microwave loss processes and nonlinear spin wave interactions, both for ferrites in general and for thin films in particular. These include (1) a general formulation of the theory of magnetostatic waves in anisotropic magnetic materials, (2) theoretical analysis of spin wave instability processes, both first and second order, for materials with a general ellipsoidal shape, a general anisotropy, and a general pumping field configuration, (3) direct identification of the spin wave interactions responsible for the onset of nonlinear loss in ferrites at high power, and (4) practical theoretical models of the two magnon scattering interaction and calculations of the resulting linewidths and off resonance losses in ferrite materials. A significant part of this work has also been accomplished under ONR support.

The previous phase of this continuing ONR program under N00014-06-1-0889 reported new results on the static and microwave properties of composite ferrite-ferroelectric materials, nonlinear and high power properties of ferrite and metallic films, low field loss properties of microwave ferrites, and new theoretical approaches for the analysis of microwave loss in magnetic materials. See Final Report dated 29 November 2007.

This phase of the ONR program achieved new results in several areas. The results include the experimental and theoretical verification of loss processes in metallic films, the development of in-plane c-axis barium hexaferrite films for millimeter wave device applications, the demonstration of a record electric field tuning response for the ferromagnetic resonance line in a ferrite yttrium iron garnet (YIG) film - ferroelectric barium strontium titanate film heterostructure, new results on loss mechanisms in ultra-dense bulk polycrystalline YIG materials, and the first experimental confirmation of nonlinear three magnon confluence processes in ferrite films. The presentation of results in this Final Report is intended to be brief and succinct. Section C.2 lists personnel supported, in whole or in part, by category. Section C.3 contains a list of the six archival publications realized during this funding period.

2. Education and Human Resources

Personnel supported in whole or in part and degrees granted during the current grant period are indicated below:

| | |
|----------------------|---|
| Visiting scientists: | 1 |
| Senior Staff | 2 |

| | |
|-------------------------------------|---|
| Postdoctoral fellows: | 4 |
| Undergraduate students: | 3 |
| High school summer apprenticeships: | 6 |

Names, degree specifics, and dates are available on request.

3. Publication list

"Microwave damping in polycrystalline Fe-Ti-N films - physical mechanisms and correlations with composition and structure," S. Kalarickal, P. Krivosik, J. Das, K. S. Kim, and C. E. Patton, Phys. Rev B77, 054427 1 to 9 (2008). February 2008

"In-plane c-axis oriented barium ferrite films with self-bias and low microwave loss, " Y. Y. Song, J. Das, Z. Wang, W. Tong, and C. E. Patton, Appl. Phys. Let. 93, 172503 (2008). October, 2008

"Electric field tunable low loss multiferroic ferrimagnetic-ferroelectric heterostructures, " By J. Das, Y. Y. Song, N. Mo, P. Krivosik, and C. E. Patton, Adv. Materials, submitted in 2008, in press (2009).

"Ferromagnetic resonance linewidth mechanisms in polycrystalline ferrites -the role of grain-to-grain and grain boundary two magnon scattering processes," S. Kalarickal, N. Mo, P. Krivosik, and C. E. Patton, Phys. Rev B, submitted in 2008, in press (2009).

"Recent advances in processing and applications of microwave ferrites," V. G. Harris, A. Geiler, Y. Chen, S. D. Yoon, M. Wu, A. Yang, Z. Chen, P. He, P. V. Parimi, X. Zuo, C. E. Patton, M. Abe, O. Acher, and C. Vittoria, J. Magn. Magn. Mat., in press (2009). (not included in reprint/preprint attachments)

"Three-magnon splitting and confluence processes for spin-wave excitations in yttrium iron garnet films - Wave vector selective Brillouin light scattering measurements and analysis, " C. L. Ordóñez-Romero, B. A. Kalinikos, P. Krivosik, Wei Tong, P. Kabos, and C. E. Patton, Phys. Rev B, submitted (2009).

Microwave damping in polycrystalline Fe-Ti-N films: Physical mechanisms and correlations with composition and structure

Sangita S. Kalarickal,¹ Pavol Krivosik,^{1,2} Jaydip Das,¹ Kyoung Suk Kim,³ and Carl E. Patton¹

¹Department of Physics, Colorado State University, Fort Collins, Colorado 80523, USA

²Slovak University of Technology, 81219 Bratislava, Slovakia

³Department of Materials Science and Engineering, Korea University, Seoul 136-701, Korea

(Received 30 October 2007; published 21 February 2008)

Ferromagnetic resonance (FMR) derivative linewidths were measured from 3 to 12 GHz on 50 nm thick sputtered polycrystalline Fe-Ti-N films with 3 at. % titanium and a nitrogen content (x_N) from 1.9 to 12.7 at. %. The measurements were made with both stripline and waveguide FMR spectrometers. Linewidths were generally lowest at $x_N=7$ at. %, with derivative linewidth (ΔH) values in the 15–25 Oe range and a nominally linear increase with frequency (f). This minimum linewidth composition is connected with the bcc to bct structural transition in the Fe-Ti-N system. Linewidths increased at both larger and smaller x_N values and were accompanied by the development of a more rounded frequency profile that is indicative of two-magnon scattering. All of the ΔH vs f data could be fitted successfully with a constant inhomogeneity broadening linewidth of 8–11 Oe, a two-magnon scattering (TMS) linewidth from the random grain-to-grain fluctuations in the effective anisotropy field directions for the polycrystal, and a magnon-electron (m-e) intrinsic relaxation term modeled through Gilbert damping with a single α value of 0.003. The actual fits were done through the convolution of a Gaussian linewidth for the inhomogeneity term and a Lorentzian linewidth for the TMS and m-e terms. The fitted anisotropy field parameters from the TMS analysis ranged between 398 and 883 Oe, with the minimum also at the bcc to bct structural transition at $x_N=7$ at. %.

DOI: 10.1103/PhysRevB.77.054427

PACS number(s): 76.50.+g, 75.50.Bb, 75.30.Ds

I. INTRODUCTION

Fe-X-N thin films, where X denotes Al, Ti, or Ta, for example, have been a subject of recent interest due to the large saturation magnetization, high initial permeability, and low coercive force in this system.^{1–8} Nanocrystalline Fe-X-N alloy films, moreover, provide an attractive option for high frequency and high speed applications for microwave devices and information storage. While some important connections between film composition, crystal structure, microstructure, static magnetic properties, and magnetodynamic properties have been reported,^{2,3,7–9} there are serious gaps in the understanding of the microwave loss.

The goal of the present work was to study the microwave damping properties in soft, polycrystalline Fe-Ti-N thin films as a function of frequency and nitrogen content. This work connects the change in structure and anisotropy with nitrogen to the magnetodynamics and, in particular, to the ferromagnetic resonance (FMR) linewidth. Specifically, the room temperature FMR response was measured as a function of frequency from 3 to 12 GHz for in-plane magnetized films with 3 at. % titanium and 1.9–12.7 at. % nitrogen. The line shapes show a more Gaussian than Lorentzian character at low frequency and a more Lorentzian than Gaussian character at high frequency. This observation leads to the use of a convolution approach to the overall linewidth analysis. The linewidth data were fitted to a combination of three processes: line broadening induced by inhomogeneities, two-magnon scattering due to randomly oriented grains in the polycrystal, and intrinsic Gilbert damping. The analysis indicates that these processes quantitatively define the overall loss picture and that two-magnon processes dominate. The extracted fit parameters correlate well with the expected

structural changes with nitrogen content and static magnetic parameters.

The paper is organized as follows. Section II gives a brief review of past work on the Fe-Ti-N thin film system. Section III describes the thin film materials and gives details on the experimental setup. Section IV presents the experimental FMR linewidth results. This includes example absorption derivative profiles and Gaussian and Lorentzian best fits to these profiles, as well as data on linewidth vs frequency and nitrogen content. Section V considers line shapes and linewidths for inhomogeneous line broadening and *bona fide* relaxation processes, reviews the theoretical basis for the mechanisms of choice used here, and gives working equations for the linewidth analysis. Section VI presents theoretical fits to the data and discusses the different linewidth contributions as they relate to inhomogeneities, two-magnon scattering, and intrinsic losses. Section VII provides a summary and conclusion.

II. BRIEF NOTE ON STRUCTURE AND LINEWIDTH CONNECTIONS

Previous work on Fe-X-N alloy films has shown that there is a transition from a body centered cubic (bcc) structure to a body centered tetragonal (bct) structure at a nitrogen concentration (x_N) of about 7 at. %.^{3,4,10,11} In a recent paper, Das *et al.*¹² have also established connections between the structural transition and a concomitant decrease in cubic anisotropy and increase in uniaxial anisotropy as the nitrogen level is increased. The operational anisotropy, cubic or uniaxial, is minimum at around 7 at. %.

While the above results, especially the data from Ref. 12, demonstrate the structural, crystallographic, and static mag-

TABLE I. Summary of parameters for the Fe-Ti-N films.

| Nitrogen content x_N (at. %) | Grain size ξ (nm) | Saturation induction $4\pi M_s$ (kG) | FMR linewidth at 9.5 GHz ΔH (Oe) |
|--------------------------------------|-----------------------------|--|--|
| 1.9 | 20 | 19.0 | 76 |
| 3.9 | 15 | 18.8 | 57 |
| 5.4 | 10 | 18.2 | 46 |
| 7 | 8.5 | 16.8 | 27 |
| 8.4 | 7.5 | 15.3 | 27 |
| 12.7 | 4 | 13.9 | 32 |

netic property connections, similar links with dynamic properties are not yet clear. These systems do show relatively low FMR linewidths⁹ that (1) decrease as x_N increases and (2) appear to correlate with the corresponding decrease in grain size. References 8 and 12 also suggest a possible connection between linewidth and magnetization ripple in thin films. The above cited FMR linewidth work, although somewhat limited, provides a natural lead into the present work. These results, described below, elucidate the connections between grain size, structural changes, and linewidth. To a large extent, these results also resolve the predominant two-magnon and inhomogeneity broadening contributions to the FMR linewidth in the Fe-Ti-N thin film system.

III. SAMPLE PROPERTIES AND FERROMAGNETIC RESONANCE MEASUREMENT TECHNIQUES

As with the work in Ref. 12, the polycrystalline Fe-Ti-N films were provided by C. Alexander, Jr. of the University of Alabama. The 50 nm thick films were prepared by dc magnetron sputtering on glass substrates. A dc magnetic field of about 300 Oe was applied in the plane of the substrates during sputtering to induce uniaxial anisotropy. All films had about 3 at. % Ti. The samples had x_N values of 1.9, 3.9, 5.4, 7.0, 8.4, and 12.7 at. %. The compositions were determined by x-ray photoelectron spectroscopy. The average grain size, as determined by transmission electron microscopy, ranged from 20 nm at $x_N=1.9$ at. % to about 4 nm at $x_N=12.7$ at. %. Preparation details are given in Ref. 2. A thorough discussion of the static magnetic properties and connections with structure is given in Ref. 12.

Table I lists key sample parameters. The x_N and grain size (ξ) values are from Ref. 2. The saturation induction ($4\pi M_s$) values are from Ref. 12. The listed 9.5 GHz FMR derivative linewidth (ΔH) values are from the present measurements. Note that saturation induction, grain size, and linewidth values generally decrease with increasing nitrogen content. This listing also demonstrates the relatively low ΔH values for the Fe-Ti-N film system.

Two systems were used for the linewidth measurements, a broadband stripline transmission spectrometer^{13,14} for 2–7 GHz and a shorted waveguide reflection spectrometer^{15,16} for 8–12 GHz. The FMR absorption de-

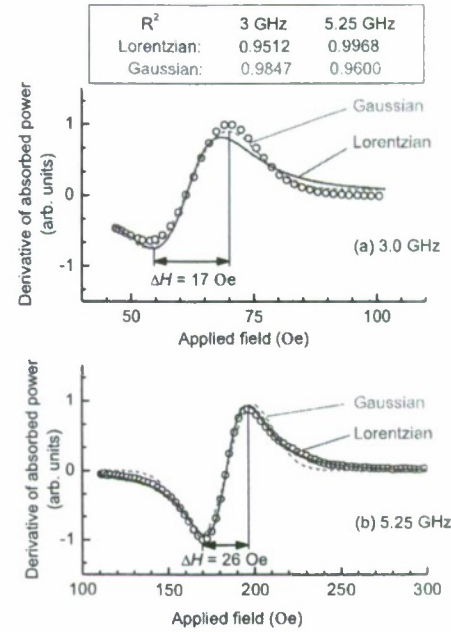


FIG. 1. (Color online) (a) and (b) show example ferromagnetic resonance absorption derivative vs field profiles for the film with $x_N=5.4$ at. % at 3.0 and 5.25 GHz, respectively. The dashed (red) and solid (blue) curves show Gaussian and Lorentzian fits to the data. The top table lists the regression parameters (R^2) for the four fits.

ivative vs field profiles were generally undistorted. The FMR derivative linewidth, taken here as ΔH , was measured as the difference between the extrema of the FMR profile. The variation in these linewidths with frequency and nitrogen content, along with the analysis of these data in terms of basic loss and line broadening processes, is the focus of this work. It is to be emphasized that all experimental and theoretical linewidths presented here are given as derivative linewidths.

IV. FERROMAGNETIC RESONANCE LINEWIDTH RESULTS

Figure 1 shows example FMR absorption derivative profiles for the sample with $x_N=5.4$ at. % at 3.0 and 5.25 GHz. The open circles show the data. The dashed and solid curves, respectively, show Gaussian and Lorentzian derivative fits to the data. For this presentation, the standard regression parameter R^2 is used as a measure of the goodness of the fits. A perfect fit would correspond to $R^2=1$. These profiles demonstrate two things. First, one can see that the resonances are reasonably sharp and symmetric, with relatively narrow linewidths, as indicated. The second point concerns line shapes. One can see that for the 3.0 GHz data in Fig. 1(a), the Gaussian fit is better than the Lorentzian fit, and for the 5.25 GHz data in Fig. 1(b), the Lorentzian fit is better. While these differences are visible from the fits shown, the variation in the goodness of the fits shows up quite strongly in the listed R^2 values. These clear differences provide the motivation for

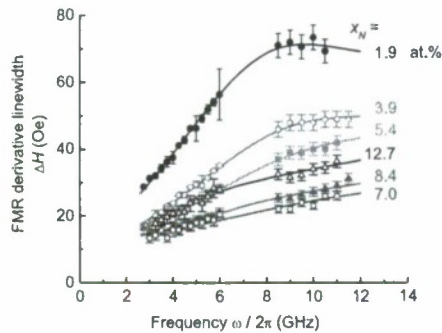


FIG. 2. (Color online) FMR derivative linewidth ΔH vs frequency ($\omega/2\pi$) for all samples. The symbols show the data for different nitrogen contents, as indicated. The curves show model fits to the data based on the theoretical considerations discussed in the text.

the convolution approach to the linewidth analysis used below.

Figure 2 shows the FMR derivative linewidth ΔH as a function of frequency ($\omega/2\pi$) for all samples. The symbols show the data for the different nitrogen levels, as indicated. The curves show fits to the data, based on theoretical considerations of two-magnon scattering, inhomogeneous line broadening, and intrinsic magnon-electron (m-e) scattering processes. The theory and fits are discussed in Secs. V and VI. Note that the frequency ω , specified in rad/s, plays an important role in the theoretical discussion to follow. The frequency parameter used for presentations of the data will usually be given in practical units as GHz.

There are two important points to be noted from Fig. 2. First, it is clear that the linewidth is not a linear function of frequency. While it is true that single crystal films and thin polycrystalline films can show a linear ΔH vs ω signature,^{14,17-19} this cannot be taken as a general statement.²⁰⁻²² From the data, one can see that the response is closest to linear for an intermediate nitrogen level at $x_N \approx 7$ at.%. This composition also corresponds to the point where the linewidth is a minimum. As one goes below or above this level, one obtains larger linewidths and a more accentuated curved response. These effects are larger for x_N values below 7 at.% than for $x_N > 7$ at.%. Figure 3 shows the data of Fig. 2 in a ΔH vs x_N format for three selected frequencies, as indicated. In this format, the data demonstrate

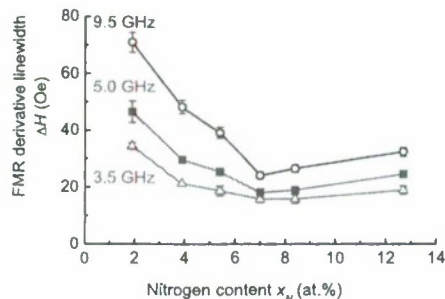


FIG. 3. (Color online) FMR derivative linewidth ΔH vs nitrogen content x_N at three selected frequencies, as indicated.

explicitly the linewidth minimum at $x_N \approx 7$ at.% and the more rapid rate of change for $x_N < 7$ at.% noted above.

The data shown in Figs. 2 and 3 can be understood in terms of the static magnetic and structural properties of the films. Inhomogeneous line broadening contributes a frequency and composition independent background linewidth. The linewidth minimum at $x_N \approx 7$ at.% is related to the established structural transition at this composition³ and a minimum value for the overall magnetic anisotropy of the films.¹² The increases in linewidth above and below the $x_N \approx 7$ at.% point as well as the enhanced curvature of the ΔH vs ω response are due to two-magnon scattering (TMS).²³⁻²⁶ These changes are related to the increase in anisotropy¹² and grain size changes. The remaining linewidth component follows the well established Gilbert (G) phenomenological model with a single, composition independent α value of 0.003. This α value is consistent with intrinsic magnon-electron scattering, the main intrinsic relaxation process for ferromagnetic resonance in metallic films.²⁷⁻³⁰

The next section provides an overview of these three linewidth mechanisms and develops working equations for fits to the data. Section VI presents the results of these fits and discusses the role of the different mechanisms.

V. LINEWIDTH MECHANISMS AND WORKING EQUATIONS

The most important point to note at the outset of this section is that inhomogeneities and physical loss processes lead to different line shapes, and one cannot simply add these two different types of linewidths to obtain a total linewidth. To lowest order, the effect of inhomogeneities amounts to the superposition of many local FMR absorption profiles with some spread in FMR fields that define the extent of the inhomogeneity. For random inhomogeneities, the spread will follow a Gaussian distribution. The corresponding FMR linewidth will, in the small signal limit, also have a Gaussian shape.

The other two processes, two-magnon scattering and intrinsic magnon-electron scattering, comprise physical relaxation mechanisms. In the small signal limit and to lowest order, these processes will have Lorentzian FMR absorption profiles. Because of this basic difference, any measured linewidth will be a convolution of the Gaussian profile associated with the inhomogeneous line broadening and the Lorentzian profile associated with the relaxation processes. This type of convolution applies, of course, only if these effects are independent of each other. The fits shown in Fig. 1 support the convolution argument. From the linewidth analysis in Sec. VI, it will be shown that the inhomogeneity linewidth contribution is larger than the linewidth associated with actual relaxation processes at lower frequencies, while the opposite is true at higher frequencies. This is precisely the indication from Fig. 1.

Based on the above, consider two contributions to the FMR linewidth. There is one linewidth associated with a Gaussian profile and related to inhomogeneity (INH) line broadening, termed ΔH_{INH} . In addition, there is a second linewidth, one associated with a Lorentzian (LOR) profile

and related to relaxation processes, termed ΔH_{LOR} . In the present situation, one can write, by way of approximation, $\Delta H_{\text{LOR}} = \Delta H_{\text{TMS}} + \Delta H_G$, where ΔH_{TMS} and ΔH_G denote the respective two-magnon scattering and magnon-electron or Gilbert contributions. Techniques for the convolution of Gaussian and Lorentzian line shapes and the use of Voigt functions are well established.³¹ Here, however, the focus is on the linewidths, not on the overall shapes of the profiles. Working equations for the approximation of the derivative linewidths may be found in Ref. 31. The combined derivative linewidth ΔH takes the form

$$\Delta H \approx \frac{\Delta H_{\text{INH}}^2 + 0.909\Delta H_{\text{INH}}\Delta H_{\text{LOR}} + 0.462\Delta H_{\text{LOR}}^2}{\Delta H_{\text{INH}} + 0.462\Delta H_{\text{LOR}}}. \quad (1)$$

Note that Eq. (1) is specific to derivative linewidths. As the development below will show, the convolution of the inhomogeneous and Lorentzian contributions to the FMR response gives a good fit to the overall data. Figure 1 has already demonstrated the shift from Gaussian to Lorentzian line shapes as a function of frequency. Linewidth analyses based on a simple addition of ΔH_{LOR} and ΔH_{INH} are widely used.^{18,21,32,33} Based on the remarks above, however, it is clear that convolution represents a more consistent approach when inhomogeneity and relaxation contributions to the linewidth are both present.

Now consider the individual contributions to the overall linewidth. As noted, line broadening due to inhomogeneities arises from the simple superposition of several local FMR profiles for different regions of the sample that are shifted in field because of some change in the magnetic properties. As one example, noninteracting regions with different M_s or anisotropy values can lead to such shifts. It is the assumed random distribution in these parameters relative to some mean value that gives rise to the overall Gaussian character of the line shape.

Inhomogeneous line broadening can take many forms. In polycrystalline ferrites with a random distribution of single crystal grains, for example, the line shape will map the random orientations of the crystallographic easy axes of the grains.²³ To lowest order, the corresponding spread in FMR fields will give a constant ΔH_{INH} that is independent of frequency. This model appears to apply to the present data. More complicated inhomogeneity line broadening models have also been proposed. These include a field dependent line broadening effect related to magnetization ripple.⁹ A brief discussion of the ripple option will be given at the end of Sec. VI.

In addition to the conceptually simple Gaussian line broadening effects discussed above, inhomogeneities can also give rise to a Lorentzian linewidth contribution related to the scattering of spin waves that are at the same frequency as the driven FMR mode. The relaxation mechanism associated with this process is called two-magnon scattering. The process was discovered in the late 1950s and early 1960s in connection with FMR loss studies in bulk ferrites.^{13,23,34,35} In this same time frame, TMS processes were also proposed as a possible linewidth mechanism in thin films.^{13,36} In recent years, there has been a renewed interest in TMS processes in

metallic ferromagnetic films, driven mainly by applications in high density and high speed magnetic recording.^{21,24,37–40}

Briefly stated, TMS processes are related to short wavelength fluctuations in the local effective field in a given sample that break the orthogonality of the FMR mode and other degenerate spin wave modes. Examples can include the grain-to-grain fluctuations in the effective magnetocrystalline anisotropy field for a polycrystalline sample with randomly oriented grains, small pores or second phase material, and surface defects. Such fluctuations can lead to a coupling between the driven FMR mode and degenerate spin wave modes, and provide a channel for TMS relaxation. The corresponding linewidth will be strongly dependent on the density of states for degenerate spin wave modes and, hence, the shape of the spin wave band. The strongest coupling is usually for spin waves with wavelengths that are well above the size of the inhomogeneity. The process cuts off for wavelengths much shorter than the inhomogeneity size. For the 5–20 nm or so grain sizes applicable here, the cutoff will be for a spin wave wave number k on the order of 10^6 – 10^7 rad/cm. This is precisely the range of the available modes for the present Fe-Ti-N films at microwave frequencies.

The thin film TMS theory used here is based on the classical analysis developed in Ref. 24. References 24 and 25 provide a qualitative introduction to thin film TMS processes in general, details on the theory, and working equations for practical calculations and fits to linewidth data. Brief comments are given below. Working equations for the linewidth calculations are given in the Appendix.

For a tractable analysis, one usually invokes the thin film approximation introduced by Harte,⁴¹ in which the spin wave modes are taken to have no spatial variation over the film cross section. In this limit, the thin film TMS linewidth developed in Ref. 25 may be cast in the form

$$\Delta H_{\text{TMS}} = \frac{1}{\sqrt{3}} \frac{|\gamma| H_A^2 \xi^2}{P_A(\omega)} \int \Lambda_{0k} C_k(\xi) \delta(\omega - \omega_k) d^2k. \quad (2)$$

Here, H_A denotes an effective anisotropy field for the randomly oriented grains defined through $H_A = 2K/M_s$, where K is an as yet unspecified anisotropy energy density for the material of interest. In Sec. VI, both cubic and uniaxial anisotropy contributions will be considered. The ξ parameter denotes the mean grain size. The $P_A(\omega)$ function is equal to $(\partial\omega_{\text{FMR}}/\partial|\gamma|H)$ evaluated at $H = H_{\text{FMR}}$, where ω_{FMR} is the field dependent FMR angular frequency and H_{FMR} is the resonance field at the operating frequency. The γ parameter denotes the gyromagnetic ratio. The P_A divisor in Eq. (2) accounts for the conversion between frequency and field swept linewidths.¹⁴ The $C_k(\xi)$ is the Fourier transform of the grain-to-grain dynamic internal field correlation function for the sample. Detailed considerations of $C_k(\xi)$ based on the anisotropy in a system of randomly oriented grains are given in Ref. 25. This $C_k(\xi)$ provides a specific form for the k dependence of the scattering for a given ξ value. The Λ_{0k} takes into account the averaging of the anisotropy axis fluctuations over the sample and the ellipticity of the precession response for both the uniform mode and the spin wave

modes. The integral folds in the scattering from the uniform mode to all available degenerate spin wave modes. The delta function $\delta(\omega - \omega_k)$ serves to select out these degenerate modes.

A full discussion of the dependences of the two-magnon linewidth on frequency, grain size, and other magnetic properties is beyond the scope of this paper. The key points for the present work are the following: (1) the different terms in Eq. (2) can lead to a complicated dependence of the two-magnon linewidth with frequency and grain size, and (2) the $\Delta H_{\text{TMS}}(\omega)$ response is, in general, not linear. As shown in the next section, the explicit nonlinear $\Delta H_{\text{TMS}}(\omega)$ response for these Fe-Ti-N films plays a crucial role in the explanation of the overall linewidth.

While two-magnon scattering is a physical relaxation process, it is based on the presence of inhomogeneities and can be taken as nonintrinsic. The last process needed for the present analysis is m-e scattering. This is the sole intrinsic relaxation process considered here. From the m-e consistent Gilbert model, one obtains a linewidth, taken here as ΔH_G , that takes the form

$$\Delta H_G = \frac{2}{\sqrt{3}} \frac{\alpha \omega}{|\gamma|}. \quad (3)$$

The linear increase in linewidth with frequency implicit in the Gilbert form has been widely observed in ferromagnetic metals.^{14,19} As noted above, the Gilbert phenomenology is also consistent with the physical relaxation process of magnon-electron scattering. Recent ab initio band structure calculations of the m-e relaxation rates for iron, cobalt, and nickel give Gilbert damping α values that are consistent with the present results as well as with the other data cited above.²⁸ The $\sqrt{3}$ divisor in Eqs. (2) and (3) accounts for the conversion between a half-power linewidth and the derivative linewidth considered here, under the assumption of a Lorentzian absorption profile.

VI. LINEWIDTH ANALYSIS AND PHYSICAL CONNECTIONS

Section V reviewed the INH, TMS, and G contributions to the FMR linewidth, with an emphasis on the possible frequency dependences of these linewidth terms as they relate to the present data. This section presents explicit theoretical fits to the linewidth data from Sec. IV. The results provide a self-consistent explanation of the FMR linewidth for this series of Fe-Ti-N thin films. The overall fits are based on the convolution of the Gaussian inhomogeneity line broadening term with a combined Lorentzian term comprised of two-magnon scattering and magnon-electron relaxation. The correlation between the extracted TMS anisotropy scattering field parameter and composition provides particularly strong evidence for the importance of two magnon scattering in these films.

Figure 4 shows the ΔH vs frequency data from Fig. 2 for $x_N = 1.9$ at. %, along with computed curves for the INH, TMS, and G linewidth contributions as well as the total fitted linewidth. The open circles denote the data; the dotted,

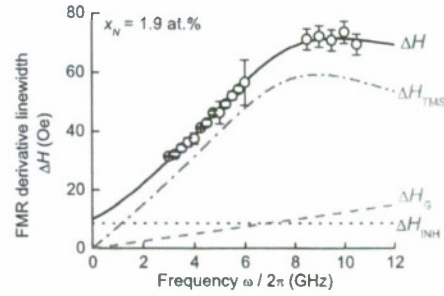


FIG. 4. (Color online) FMR derivative linewidth ΔH vs frequency $(\omega/2\pi)$ for $x_N = 1.9$ at. %. The open circles show the data. The dotted (blue), dashed (red), and dot-dashed (green) lines show the computed inhomogeneity, Gilbert, and two-magnon scattering linewidth components, respectively. The solid (black) curve shows the combined linewidth according to Eq. (1).

dashed, and dot-dashed curves show the INH, TMS, and G linewidths, respectively; and the solid curve shows the total fitted linewidth. It was observed that fits with Gilbert α as a free parameter yielded the value of α for all samples as 0.003 ± 0.0002 . The computed curves were obtained with the applicable parameter values from Table 1 and, as noted above, a free electron $|\gamma|/2\pi$ value of 2.8 GHz/kOe and a Gilbert α value of 0.003. Following Ref. 12, the anisotropy type for $x_N = 1.9$ at. %, needed for the TMS Λ_{0k} function, was taken as cubic and the exchange energy parameter A was taken as 3×10^{-6} erg/cm. The ΔH_{INH} and H_A were taken as fitting parameters. The curves shown are for $\Delta H_{\text{INH}} = 10$ Oe and $H_A = 779.7$ Oe. The regression parameter R^2 for the fit shown is 0.996.

Apart from the good theoretical fits, Fig. 4 shows three things. First, one can see that the convolution combines the three component linewidths to give an overall ΔH vs frequency response with a small upward curvature at low frequency. While this is clearly a small effect, it could turn out to be significant if the measurements could be extended to lower frequencies. This and related points will be considered at the end of the section.

The second point is that the dominant overall linewidth process, especially at the higher frequencies, is two-magnon scattering. The data and the fits show that this linewidth contribution has a somewhat complicated frequency dependence, with a linear increase at low frequency, a broad maximum of 8–10 GHz, and a small drop at higher frequencies. The signature of two-magnon scattering is very different from the simple linear response implicit in the Gilbert model. Based on the good fit shown here, it is clear that there can be no justification for the wide spread use of the Gilbert model to “explain” FMR linewidths in metallic films, often without any realistic consideration of the physical origins of these linewidths. The third point is that the fitted α value of 0.003 is consistent with expected values for m-e scattering in metallic films.^{27–29}

Figure 5 shows all of the ΔH vs frequency data from Fig. 2, broken out into separate graphs for all the samples, along with curves for the overall linewidth fits. The open circles show the data and the solid curves show the fits. Apart from the previously noted common value of α (0.003) used for all

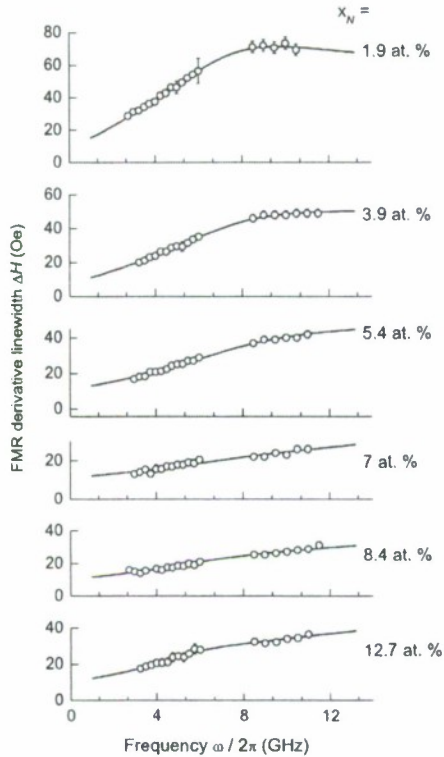


FIG. 5. FMR derivative linewidth ΔH vs frequency for all the samples. The solid curves give the calculations of the linewidth with the inhomogeneity line broadening, the two-magnon scattering, and the Gilbert damping contributions to the total linewidth.

fits, the curves in Fig. 5 are based on the parameters from Table I and the additional linewidth fitting parameters given in Table II. As with the data in Fig. 4, a constant background inhomogeneity linewidth ΔH_{INH} has been used for each graph, according to the values in Table II. Note that the exchange stiffness constant A was taken at 3×10^{-6} erg/cm for the films with $x_N \leq 7$ at.%,¹² and reduced to 2×10^{-6} and 1×10^{-6} erg/cm for the samples with $x_N = 8.4$ and 12.7 at.%, respectively. In view of the bcc to bct structure change at $x_N \approx 7$ at.%, this change is reasonable.

One can also see from Table II that the fitted H_A values show a minimum at $x_N \approx 7$ at.% and then increase as one goes above or below this composition. Keep in mind that the

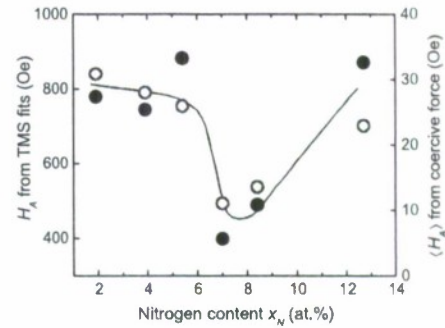


FIG. 6. (Color online) Anisotropy field parameter values as a function of the nitrogen content x_N . The solid (black) circles and left side axis show the H_A values from Table II. The error bars are on the order of the size of the points. The open (blue) circles and right side axis show the averaged anisotropy $\langle H_A \rangle$ values taken from Ref. 12. The solid curve serves as a guide for the eye for the trend of the data.

two-magnon fits are based on cubic anisotropy working equations for x_N values below 7 at.% and on uniaxial anisotropy for values of 7 at.% and above. This is indicated in the fifth column of Table II. These anisotropy details are significant for the discussion below.

The trend of the data with film composition was discussed in connection with Fig. 3. Here, the focus is on the trend of the fits with composition and the two-magnon scattering implications. Note that all of the fits are quite good. The regression R^2 values listed in Table II are all reasonably close to unity. The two-magnon part of the linewidth, mainly connected with the ΔH vs frequency dependences that deviate from a simple linear behavior, starts out large at $x_N = 1.9$ at.%, initially drops off as x_N increases, is minimum for the $x_N = 7$ and 8.4 at.% samples, and then becomes slightly larger as x_N moves toward 12.7 at.%.

The most important result from Fig. 5 and Table II relates to the minimum two-magnon linewidth contribution for $x_N = 7$ at.% and the correlations with anisotropy and structural change. Figure 6 captures these results succinctly. The solid points show the H_A values as a function of x_N from Table II. The open circles show companion effective anisotropy data from Ref. 12. These latter data derive from coercive force measurements on these same samples and extractions of an effective cubic or uniaxial anisotropy energy density param-

TABLE II. Summary of fit parameters.

| Nitrogen content x_N (at. %) | Inhomogeneity broadening ΔH_{INH} (Oe) | Exchange constant A ($\times 10^{-6}$ erg/cm) | Anisotropy field H_A (Oe) | Anisotropy type | Fit regression R^2 |
|--------------------------------------|---|--|-----------------------------------|-----------------|-------------------------|
| 1.9 | 10.0 ± 0.8 | 3.0 | 779.7 ± 4.0 | Cubic | 0.996 |
| 3.9 | 8.3 ± 0.5 | 3.0 | 745.1 ± 4.1 | Cubic | 0.997 |
| 5.4 | 11.0 ± 0.4 | 3.0 | 882.6 ± 8.6 | Cubic | 0.993 |
| 7 | 11.3 ± 0.5 | 3.0 | 398.4 ± 24.9 | Uniaxial | 0.939 |
| 8.4 | 10.5 ± 0.5 | 2.0 | 489.4 ± 13.7 | Uniaxial | 0.976 |
| 12.7 | 10.4 ± 0.7 | 1.0 | 871.6 ± 16.1 | Uniaxial | 0.982 |

eter, denoted here as a generic $\langle K \rangle$. The $\langle H_A \rangle$ values shown in the figure derive from an anisotropy connection of the form $\langle H_A \rangle = 2\langle K \rangle / M_s$. Following Ref. 12, and in the spirit of the two-magnon analysis here, the values for $x_N \leq 7$ at.% correspond to cubic anisotropy and those for $x_N > 7$ at.% to uniaxial anisotropy. Note that the right side $\langle H_A \rangle$ scale in Fig. 6 differs from the left side H_A scale by a factor of 30–80. This difference in scale is discussed in Ref. 12. The curve through the ensemble of data points is intended as a guide for the eye.

Figure 6 makes explicit the minimum in the H_A values from the two magnon fits at $x_N \approx 7$ at.%. It also demonstrates the consistency between these data and the averaged $\langle H_A \rangle$ results from Ref. 12. These results, in combination with the good match between experiment and theory in Fig. 5, provide convincing arguments for (1) a strong composition dependent two-magnon contribution to the linewidth, (2) clear correlations with a structure change at $x_N \approx 7$ at.%, and (3) quantitative fits that support the use of a bcc model below and a bct model above the transition point. As one such quantitative point of comparison, the cubic anisotropy energy density parameter from the TMS fit for $x_N \approx 1.9$ at% is obtained as 590×10^3 erg/cm³. The literature value for pure iron is about 480×10^3 erg/cm³.⁴²

Up to now, there has been no comment on the role of grain size on the calculated TMS linewidth. As evident from Eq. (2), the grain size ξ enters the TMS analysis both as a prefactor and as a parameter inside the correlation integral. The grain size, however, was not taken as a fitting parameter. All of the fits were based on the measured grain sizes from Ref. 12, as listed in Table I. It turns out that any small change in grain size from these measured values causes a significant degradation in the best fit matchup with the data. This means, in turn, that the “best fit” ξ value matches up nearly perfectly with the measured grain size. This lends additional credence to the two magnon linewidth results presented above.

As noted in Sec. V, a field dependent inhomogeneity line broadening mechanism related to magnetization ripple has also been proposed. Reasonable fits to the present data could also be obtained from this model, the working equations in Ref. 9, and the averaged effective uniaxial anisotropy field determinations from Ref. 12. With this approach, the R^2 values for fits based on a ripple inhomogeneity line broadening are about the same as those in Table II for a constant ΔH_{INH} . From these results, one could argue that magnetization ripple is a reasonable source of the ΔH_{INH} . Such a mechanism can be justified here because ripple line broadening has a very weak dependence on the applied field in the FMR regime of fields and frequencies studied here. On the other hand, the ripple model also predicts a very rapid increase in the inhomogeneity linewidth at frequencies below 2 GHz. Up to now, there is no evidence for such a response at low frequency.

VII. SUMMARY AND CONCLUSION

In summary, the above sections have described 3–12 GHz ferromagnetic resonance linewidth measurements and analyses for a series of polycrystalline Fe-Ti-N films

TABLE III. Averaging coefficients for the variation in the anisotropy direction.

| Type of anisotropy | Averaging coefficients | | | |
|--------------------|------------------------|--------|-------|-------|
| | c_1 | c_2 | c_3 | c_4 |
| In-plane uniaxial | 1/8 | 3/32 | 0 | 1/8 |
| First order cubic | 29/420 | 29/420 | 3/140 | 1/105 |

with nitrogen concentrations (x_N) ranging from 1.9–12.7 at.%. The data show clear departures from the linear linewidth vs frequency response that is usually taken as the norm for metallic films. The linewidths generally show a minimum at the bcc to bct structural transition point at $x_N \approx 7$ at.%.

A model with three terms, a constant inhomogeneous broadening linewidth, a two-magnon scattering linewidth term, and an intrinsic magnon-electron term modeled through a Gilbert damping form, gives good fits to the data. The particular fits obtained here were based on the convolution of a Gaussian form for the inhomogeneous term and a Lorentzian for the two remaining physical processes. The fitted two-magnon term gives values of the effective anisotropy field in the grains that are consistent with previous reports and correlate with the structural transition noted above.

ACKNOWLEDGMENTS

This work was supported in part by the Office of Naval Research (USA) Grant No. N00014-06-1-0889, the U.S. Army Research Office, MURI Grant No. W911NF-04-1-0247, the Information Storage Industry Consortium (INSIC) Extremely High Density Recording (EHDR) program, and Seagate Technologies. The samples and the grain size analysis were provided by J. C. Alexander, Jr., MINT Center, University of Alabama.

APPENDIX

This appendix gives working equations for the evaluation of the terms in Eq. (2) for the two-magnon scattering field swept linewidth ΔH_{TMS} . These equations are specific to an in-plane magnetized thin film with an average grain size ξ , taken here to be the same as the correlation length for the grain-to-grain fluctuation in the effective anisotropy field. All of the applicable parameters have been defined in the discussion of Eq. (2). For readability, some of these definitions are repeated below.

The Fourier transform of the grain-to-grain effective field correlation function, $C_k(\xi)$, is taken to have the form

$$C_k(\xi) = \frac{1}{[1 + (k\xi)^2]^{3/2}}, \quad (\text{A1})$$

where $k=|\mathbf{k}|$ is the spin wave wave number. In real space, this corresponds to a point-to-point effective field correlation

that falls off as $e^{-|\mathbf{r}-\mathbf{r}'|/\xi}$, where \mathbf{r} and \mathbf{r}' represent two separate positions in the film.²⁴

The ellipticity function $\Lambda_{0\mathbf{k}}$ is given by

$$\Lambda_{0\mathbf{k}} = c_1 e_0 e_{\mathbf{k}} + \frac{c_2}{e_0 e_{\mathbf{k}}} + c_3 \left(\frac{e_0}{e_{\mathbf{k}}} + \frac{e_{\mathbf{k}}}{e_0} \right) + c_4. \quad (\text{A2})$$

Here, e_0 and $e_{\mathbf{k}}$ denote the ellipticity of the uniform mode and a given spin wave mode at wave vector \mathbf{k} , respectively. These ellipticity factors are given by

$$e_0 = \sqrt{\frac{H + 4\pi M_s}{H}} \quad (\text{A3})$$

and

$$e_{\mathbf{k}} = \sqrt{\frac{H + Dk^2 + 4\pi M_s N_k}{H + Dk^2 + 4\pi M_s (1 - N_k) \sin^2 \theta_k}}, \quad (\text{A4})$$

where D is an exchange field parameter related to the exchange energy parameter A according to $D = 2A/M_s$. The thin film dipole field effective demagnetizing factor N_k is given by $N_k = (1 - e^{-kd})/kd$, where d is the film thickness,⁴¹ and θ_k is the angle between the in-plane static field direction and the in-plane wave vector \mathbf{k} direction. The c_1 , c_2 , c_3 , and c_4 parameters are connected to averages of the scattering over all of the randomly oriented grains.²⁴ The numerical values of these parameters for cubic and uniaxial anisotropies are listed in Table III. Finally, the $P_A(\omega)$ function in Eq. (2) is given by

$$P_A(\omega) = \sqrt{1 + \left(\frac{4\pi M_s}{2\omega/\gamma} \right)^2}. \quad (\text{A5})$$

- ¹D. J. Rogers, S. Wang, D. E. Laughin, and M. H. Kryder, *IEEE Trans. Magn.* **28**, 2418 (1992).
- ²Y. Ding and J. C. Alexander, *J. Appl. Phys.* **91**, 7833 (2002).
- ³Y. Ding, S. C. Byeon, and J. C. Alexander, *IEEE Trans. Magn.* **37**, 1776 (2001).
- ⁴Y. Ding and J. C. Alexander, *IEEE Trans. Magn.* **42**, 5 (2006).
- ⁵A. Chakraborty, K. R. Mountfield, G. H. Bellesis, D. N. Lambeth, and M. H. Kryder, *J. Appl. Phys.* **80**, 1012 (1996).
- ⁶B. Viala, M. K. Minor, and J. A. Barnard, *J. Appl. Phys.* **80**, 3941 (1996).
- ⁷S. C. Byeon, Y. Ding, and C. Alexander, Jr., *IEEE Trans. Magn.* **36**, 2502 (2000).
- ⁸J. Rantschler, Ph.D. thesis, University of Alabama, 2003.
- ⁹J. Rantschler and C. Alexander, *J. Appl. Phys.* **93**, 6665 (2003).
- ¹⁰A. V. Mijiritskii and D. O. Boerma, *Phys. Rev. B* **64**, 035410 (2001).
- ¹¹J. M. D. Coey and P. A. I. Smith, *J. Magn. Magn. Mater.* **200**, 405 (1999).
- ¹²J. Das, S. S. Kalarickal, K. S. Kim, and C. E. Patton, *Phys. Rev. B* **75**, 094435 (2007).
- ¹³C. E. Patton, *J. Appl. Phys.* **39**, 3060 (1968).
- ¹⁴S. S. Kalarickal, P. Krivosik, M. Wu, C. E. Patton, M. L. Schneider, P. Kabos, T. J. Silva, and J. P. Nibarger, *J. Appl. Phys.* **99**, 093909 (2006).
- ¹⁵M. J. Hurben, Ph.D. thesis, Colorado State University, 1996.
- ¹⁶J. J. Green and T. Kohane, *Semicond. Prod. Solid State Technol.* **7**, 46 (1964).
- ¹⁷C. E. Patton, Z. Frait, and C. H. Wilts, *J. Appl. Phys.* **46**, 5002 (1975).
- ¹⁸B. Heinrich, J. F. Cochran, and R. Hasegawa, *J. Appl. Phys.* **57**, 3690 (1985).
- ¹⁹B. Heinrich, R. Urban, and G. Waltersdorf, *J. Appl. Phys.* **91**, 7523 (2002).
- ²⁰J. Lindner, K. Lenz, E. Kosubek, K. Baberschke, D. Spoddig, R. Meckenstock, J. Pelzl, Z. Frait, and D. Mills, *Phys. Rev. B* **68**, 060102 (2003).
- ²¹K. Lenz, H. Wende, W. Kuch, K. Baberschke, K. Nagy, and A. Janossy, *Phys. Rev. B* **73**, 144424 (2006).
- ²²K. Zakeri, J. Lindner, I. Barsukov, R. Meckenstock, M. Farle, U. von Hörsten, H. Wende, W. Keune, J. Rocker, S. S. Kalarickal, K. Lenz, W. Kuch, K. Baberschke, and Z. Frait, *Phys. Rev. B* **76**, 104416 (2007).
- ²³E. Schloemann, *J. Phys. Chem. Solids* **6**, 242 (1958).
- ²⁴R. McMichael and P. Krivosik, *IEEE Trans. Magn.* **40**, 2 (2004).
- ²⁵P. Krivosik, N. Mo, S. S. Kalarickal, and C. E. Patton, *J. Appl. Phys.* **101**, 083901 (2007).
- ²⁶M. Sparks, *Ferromagnetic Relaxation Theory* (McGraw-Hill, New York, 1964).
- ²⁷B. Kuanr, R. Camley, and Z. Celinski, *J. Appl. Phys.* **95**, 6610 (2004).
- ²⁸K. Gilmore, Y. U. Idzerda, and M. D. Stiles, *Phys. Rev. Lett.* **99**, 027204 (2007).
- ²⁹C. Scheck, L. Cheng, and W. E. Bailey, *Appl. Phys. Lett.* **88**, 252510 (2006).
- ³⁰V. Kamberský and C. E. Patton, *Phys. Rev. B* **11**, 2668 (1975).
- ³¹A. M. Stoneham, *J. Phys. D* **5**, 672 (1972).
- ³²B. Kuanr, R. Camley, and Z. Celinski, *J. Magn. Magn. Mater.* **286**, 276 (2005).
- ³³S. Mizukami, Y. Ando, and T. Miyazaki, *Phys. Rev. B* **66**, 104413 (2002).
- ³⁴C. E. Patton, C. H. Wilts, and F. B. Humphrey, *J. Appl. Phys.* **38**, 1358 (1967).
- ³⁵E. Schloemann, AIEE Special Publication No. T-91, 1956 (unpublished), p. 600.
- ³⁶A. J. Bertaud and H. Pascard, *J. Appl. Phys.* **36**, 970 (1965).
- ³⁷R. Arias and D. L. Mills, *Phys. Rev. B* **60**, 7395 (1999).
- ³⁸R. McMichael, M. Stiles, P. Chen, and W. Egelhoff, Jr., *J. Appl. Phys.* **83**, 7037 (1998).
- ³⁹A. Y. Dobin and R. H. Victoria, *Phys. Rev. Lett.* **92**, 257204 (2004).
- ⁴⁰G. Woltersdorf and B. Heinrich, *Phys. Rev. B* **69**, 184417 (2004).
- ⁴¹K. J. Harte, *J. Appl. Phys.* **36**, 960 (1965).
- ⁴²G. Herzer, *IEEE Trans. Magn.* **26**, 1397 (1990).

In-plane *c*-axis oriented barium ferrite films with self-bias and low microwave loss

Young-Yeal Song,^{a)} Jaydip Das, Zihui Wang, Wei Tong, and Carl E. Patton
 Department of Physics, Colorado State University, Fort Collins, Colorado 80523, USA

(Received 18 August 2008; accepted 9 October 2008; published online 28 October 2008)

Hybrid pulse laser deposition and liquid phase epitaxy methods have been used to produce in-plane *c*-axis (IPCA) oriented barium ferrite (BaM) films on *a*-plane (11 $\bar{2}$ 0) sapphire substrates with low microwave loss and a high remanence. Total thicknesses were from 5 to 20 μm . A reasonable compromise for low loss and high remanence was reached at a thickness of 7 μm , with a remanence ratio of 0.84 and a 59 GHz peak-to-peak derivative linewidth of 250 Oe. The 20 μm thick film had a linewidth of 110 Oe, one of the smallest values ever obtained for IPCA BaM films. © 2008 American Institute of Physics. [DOI: 10.1063/1.3010374]

One important challenge for millimeter wave magnetic film device applications is in the development of low loss self-biased high anisotropy hexagonal ferrite films. Such films have potential uses for a wide range of monolithic microwave integrated circuit (MMIC) magnetic devices.^{1–4} The critical parameter for self-bias is a high magnetic remanence, that is, a large average magnetization for the film at zero applied field. Low microwave loss is also critical for a real device with an acceptably low insertion loss.

Hexagonal *M* type barium ferrite (BaM) films, with a high uniaxial anisotropy and an effective anisotropy field (H_A) of 17 kOe or so and a nominal saturation induction ($4\pi M_s$) of 4 kG,⁵ are good candidates for such devices. The hexagonal *c*-axis serves as the easy magnetization direction. The high anisotropy field allows one to achieve the desirable millimeter wave frequency, even in the absence of an external biasing magnet.

There has been some progress for BaM films with the *c*-axis normal to the film plane (NCA). Song *et al.*⁶ made such films by pulse laser deposition (PLD) with a near single crystal of 60 GHz ferromagnetic resonance (FMR) peak-to-peak derivative linewidth (ΔH_{pp}) of 16 Oe.⁶ The remanent magnetization (M_r), however, was quite small. Excessive stress limited film thicknesses to 0.85 μm or so. Thicker NCA BaM films have been made by a hybrid PLD liquid phase epitaxy (LPE) approach.^{7,8} A thin high quality PLD seed layer is first deposited. A second layer, up to 45 μm in thickness, is then grown by LPE methods. The nominal 60 GHz ΔH_{pp} values were in the 30–75 Oe range. The thick film remanence ratio M_r/M_s (RR)-values were near zero, as expected for high quality thick films. NCA BaM films have also been made by screen printing.^{9,10} These films had moderate loss, with nominal 60 GHz ΔH_{pp} values in the 300–500 Oe range, and a high RR in the range of 0.96 range.

The new challenge, however, is to realize in-plane *c*-axis (IPCA) films with low loss and high RR values. The basic advantage of IPCA films is in the higher ferromagnetic resonance frequency. For given magnetization and anisotropy values, the zero external field FMR frequency for RR=1 goes from $\omega_{FMR}^{NCA} = |\gamma|(H_A - 4\pi M_s)$ for a NCA film to ω_{FMR}^{IPCA}

$= |\gamma|\sqrt{H_A(H_A + 4\pi M_s)}$ for an IPCA film. Here, γ denotes the gyromagnetic ratio. For the BaM parameters cited above, the $\omega_{FMR}^{IPCA}/\omega_{FMR}^{NCA}$ enhancement factor is about 1.45. This is significant. In principle, the realization of a high RR for IPCA films is also made easier, since the in-plane demagnetizing factors for thin films are close to zero and self-demagnetization effects are minimized.

Progress for IPCA BaM films has been limited. Yoon *et al.*^{11,12} were able to make such films both on *a*- and *m*-plane sapphire substrates. High RR values above 0.9 were obtained for PLD films on *a*-plane sapphire substrates up to 7 μm or so in thickness, but the linewidths were large, in the range of kOe.¹¹ LPE films on *m*-plane sapphire appeared to have local regions with nominal 60 GHz ΔH_{pp} values below 100 Oe, but the overall linewidth was much larger and the films had relatively low RR-values.¹² Up until now, no group has been able to produce IPCA BaM films that combine both a high remanence and low loss.

Lattice mismatch and surface chemistry provide the key to successful epitaxy. From the narrow FMR linewidth in Ref. 6, it is clear that good epitaxy is achievable for NCA BaM films on sapphire substrates. The inability to produce low linewidth NCA films for thicknesses above 0.8 μm or so, however, also points to the presence of significant stress. From Refs. 11 and 12, it is clear that for IPCA films, both the *a*-plane and the *m*-plane sapphire substrate growth options present problems. For the present work, *a*-plane substrates were used, but hybrid PLD/LPE films were prepared. Relatively thin PLD BaM epitaxial films were first grown on the *a*-plane substrate. This was done in anticipation of a good RR ratio for thicker LPE films grown on the PLD seed layer in the second step. Following Refs. 7 and 8, it was also expected that the hybrid PLD/LPE approach would also yield narrow linewidths. This expectation was realized, but some fine-tuning in the process parameters was needed. It was necessary, for example, to use lower deposition temperatures for the initial PLD seed layer than normally used to make the highest quality film. It appears that some degradation in the seed layer is needed in order to get adequate strain relief for the subsequent thick LPE layer.

The hybrid approach produced IPCA oriented *m*-plane BaM films with high remanence and moderate loss. Films in the 5–7 μm thickness range appear to offer the best remanence/linewidth compromise. At 7 μm , one has RR

^{a)}Electronic mail: yysong@lamar.colostate.edu.

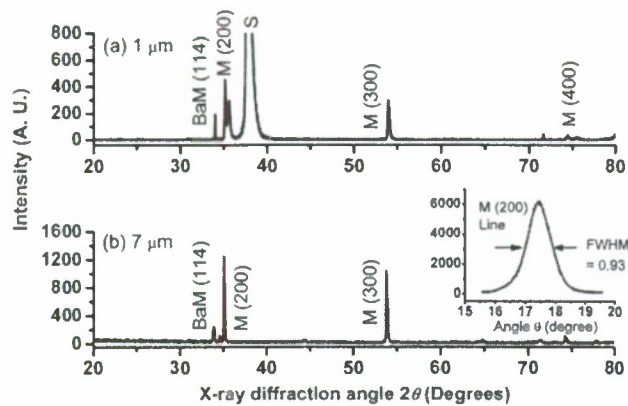


FIG. 1. (Color online) IPCA BaM film XRD 2θ scans. Graphs (a) and (b) show results for a $1\ \mu\text{m}$ thick PLD seed film and the corresponding $7\ \mu\text{m}$ thick hybrid film, respectively. The BaM, M, and S miller indices identify the important peaks, with S for the sapphire substrate and M for the characteristic m plane peaks. The (h) inset shows a rocking curve for the M (200) diffraction line.

~ 0.84 and a 59 GHz FMR ΔH_{pp} value of 250 Oe. Thicker films show a decrease in ΔH_{pp} but also a decrease in remanence. At $20\ \mu\text{m}$, one has $RR \sim 0.33$ and $\Delta H_{pp} \sim 110$ Oe. Thinner films show higher remanence values but degraded linewidths, presumably due to stress effects.

The first step was to lay down the thin seed layer. A nominal $1\ \mu\text{m}$ thick epitaxial PLD seed layer was grown on a -plane (11 $\bar{2}$ 0) sapphire. The energy fluence and repetition rate for the 248 nm KrF excimer laser was $1.7\ \text{J}/\text{cm}^2$ and 25 Hz, respectively. The deposition time was 25 min, the substrate temperature was $870\ ^\circ\text{C}$, and the target substrate distance was 6.6 cm. These conditions gave bare unannealed PLD m -plane films with $RR \sim 0.9$ and a nominal 60 GHz ΔH_{pp} of about 1.2 kOe. X-ray diffraction (XRD) data showed that higher deposition temperatures can give somewhat better epitaxy but no improvement in linewidth. It is to be emphasized that the XRD data showed the growth of m -plane films. The large linewidths are likely due to the large m -plane BaM a -plane sapphire mismatch induced strain. The overall mismatch is complicated because of the overlay of these different classes of planes.

The second step is to lay down the thicker LPE film on the seed. A mixture of BaCO_3 , Fe_2O_3 , and B_2O_3 with mole ratio of 1.0:0.25:0.571, as in Ref. 8, was mixed thoroughly at $1250\ ^\circ\text{C}$ for 6 h. The homogeneous melt was then cooled to the desired LPE growth temperature. A growth temperature of $860\ ^\circ\text{C}$, as measured with an external thermocouple, was found to give good epitaxial films. Lower temperatures gave mottled films. Higher temperatures yielded no film growth at all. As noted above, film thicknesses ranged from 5 to $20\ \mu\text{m}$. Thickness was controlled by the immersion time for the seed film in the supersaturated melt. The growth rate was about $0.2\ \mu\text{m}/\text{min}$. The film thicknesses were determined from cross section scanning electron microscopy (SEM).

Graphs (a) and (b) in Fig. 1 show standard $\theta/2\theta$ diffraction scans for a nominal $1\ \mu\text{m}$ thick PLD film and a $7\ \mu\text{m}$ thick hybrid PLD/LPE film, respectively. The inset in (b) shows the M (200) rocking curve. The diffraction peaks in (a) come mostly from the (ℓ 00) m -plane scattering of the hexagonal structure, except for a small peak from the (114) plane. One can also see the a -plane sapphire "S" peak. In (b),

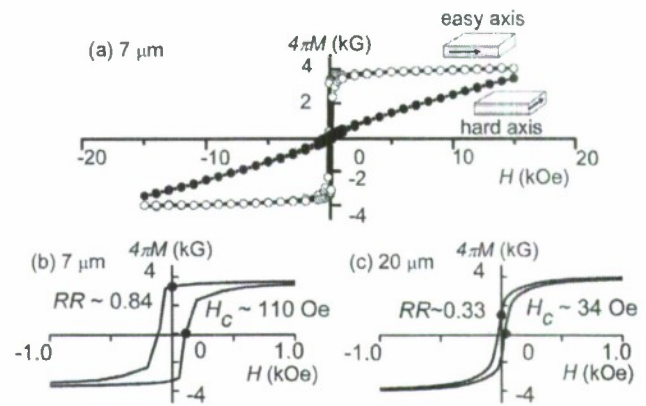


FIG. 2. (Color online) Hysteresis loops of the magnetic induction $4\pi M$ vs in-plane static field H . (a) and (b) show EA and hard axis field loops and the EA loop on an expanded field scale, respectively, for the $7\ \mu\text{m}$ thick film in Fig. 1. (c) shows the expanded EA loop for the $20\ \mu\text{m}$ film. Remanence ratios RR s and coercive fields (H_c) indicated in (b) and (c).

one sees the same (ℓ 00) m -plane reflections as in (a). Here, however, there is no sapphire peak and the intensities of the (ℓ 00) peaks in (b) are about three times higher than those in (a). The full width at half maximum of the XRD rocking curve is 0.93° . While the film is not perfectly oriented, the film is reasonably epitaxial. All told, the XRD data underscore the epitaxial growth of IPCA BaM PLD/LPE hybrid by the recipe given above.

The graphs in Fig. 2 shows representative room temperature vibrating sample magnetometry hysteresis loop data in an induction $4\pi M$ versus static field H format. The data in (a) and (b) are for the same $7\ \mu\text{m}$ film as in Fig. 1. (a) shows data with the field H applied along the in-plane (IP) easy and hard directions, as indicated. (b) shows the easy axis (EA) IP loop on an expanded field scale. (c) shows similar data as in (b) but for a $20\ \mu\text{m}$ film. The data in (a) show that the film has an in-plane uniaxial axis. The $7\ \mu\text{m}$ film saturation induction $4\pi M_s$ and effective uniaxial anisotropy field H_A values are about 3.9 kG and 17.3 kOe, respectively. These are close to the reported values for single crystal NCA BaM films.⁶ The corresponding $4\pi M$ and H_A values for the $20\ \mu\text{m}$ thick film were 4.0 kG and 17.3 kOe, respectively. The $20\ \mu\text{m}$ thick film data in (c) shows much lower coercive field and RR -values than do the $7\ \mu\text{m}$ film data (b).

Graphs (a) and (b) in Fig. 3 show in-plane EA field 59 GHz FMR data (open circles) and Lorentzian derivative fits (solid curves) for the same films as in Fig. 2, shown in an absorption derivative versus field format. The fits are reasonably good. The FMR fields for the (a) and (b) data, taken as the zero crossing points from the fits, are about 2.07 and 2.24 kOe, respectively. The derivative linewidths are as indicated in the figure. For IP EA field ferromagnetic resonance, the applicable FMR frequency (ω) field (H_0) connection is given by

$$\omega = |\gamma| \sqrt{(H_0 + H_A)(H_0 + H_A + 4\pi M_s)}, \quad (1)$$

Based on the operating frequency of 59 GHz, $|\gamma|/2\pi = 2.8\ \text{GHz}/\text{kOe}$, and the $4\pi M$ and H_A values cited above, one obtains theoretical FMR field values of 1.91 kOe ($7\ \mu\text{m}$ film) and 1.87 kOe ($20\ \mu\text{m}$ film). The matches with the data are reasonable and well within the range of error set by the uncertainties in $4\pi M$ and H_A .

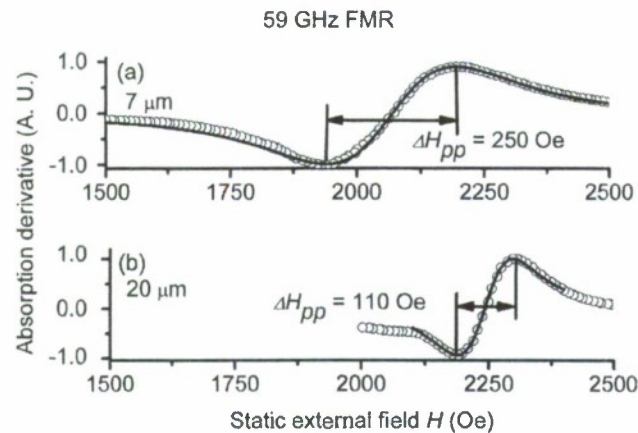


FIG. 3. Graphs (a) and (b) show 59 GHz FMR absorption derivative vs H profiles for the 7 and 20 μm thick films featured in Fig. 2, respectively. The open circles show the data. The solid curves show Lorentzian derivative best fits. The peak-to-peak derivative linewidths (ΔH_{pp}) are as indicated.

Turn now to the linewidths. Recall that the initial seed layer alone has $\Delta H_{pp} \approx 1.2$ kOe. The 250 Oe linewidth for the 7 μm hybrid film is about a factor of five smaller and the 110 Oe linewidth for the 20 μm hybrid film is more than a factor of 10 lower than the seed linewidth. It is clear that the thicker the hybrid film, the better the crystal alignment, the more the strain relief, and the better the overall film quality as measured by the linewidth.

Figure 4 shows (a) RR and (b) 59 GHz ΔH_{pp} linewidth values as a function of film thickness. From (a), one sees that the RR value decreases more or less smoothly from about 0.9 at 1 μm down to about 0.3 at 20 μm . As discussed in connection with Fig. 2, the decrease in the RR accompanied by a decrease in the coercive force as well. These decreases are tentatively ascribed mainly to the strain relief that comes

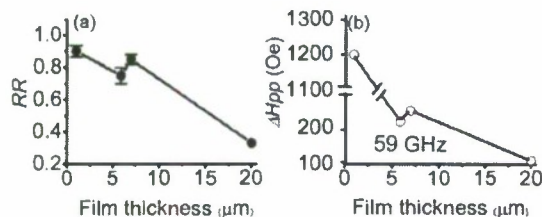


FIG. 4. (a) RR vs film thickness. (b) 59 GHz peak-to-peak derivative linewidth ΔH_{pp} vs film thickness. The data points for the 1 μm film are a pure PLD film, with the FMR measurements done at about 66 GHz.

with thicker LPE layers and the corresponding reduction in local stress related obstacles to domain wall movement. Graph (b) shows a similar trend for the linewidth. The nominal V band linewidth decreases from about 1200 Oe at 1 μm down to about 110 Oe for 20 μm thickness. Roughly speaking, one can see that a thickness around 7 μm or so offers a reasonable compromise for a high RR and low linewidth, with RR ~ 0.84 and $\Delta H_{pp} \sim 250$ Oe. Thinner films offer high RR and high loss, while thicker films offer small RR and low loss.

In summary, hybrid PLD and LPE techniques have been used to produce IPCA BaM films with low microwave loss and a high remanence. The use of an initial thin PLD seed film of moderate quality with a LPE grown thicker film on top, appears to provide a viable way to produce useful films for planar high frequency MMIC devices. It is noteworthy, moreover, that the 110 Oe derivative linewidth for the 20 μm film is one of the smallest values achieved for IPCA oriented barium ferrite film on any substrate.

This work was supported in part by the Office of Naval Research (ONR) Grant Nos. N00014-07-1-0597 and N00014-08-1-1050 (through sub-award No. PT103701-SC101157 from Virginia Commonwealth University), the ARO-DARPA Multifunctional Materials Seedling Program, Contract No. W911NF-06-1-0163, and ARO-MURI Grant No. W911NF-04-1-0247. Dr. S. Kohli and Dr. P. McCurdy are acknowledged for the XRD and SEM measurements.

¹S. Capraro, T. Rouiller, M. L. Berre, J. P. Chatelon, B. Bayard, D. Barbier, and J. J. Rousseau, IEEE Trans. Compon. Packag. Technol. **30**, 411 (2007).

²C. K. Queck and L. E. Davis, Electron. Lett. **39**, 1595 (2003).

³P. Kwan and C. Vittoria, IEEE Trans. Magn. **29**, 3431 (1993).

⁴P. Kwan and C. Vittoria, IEEE Trans. Microwave Theory Tech. **41**, 652 (1993).

⁵C. A. Carosella, D. B. Chrisey, P. Lubitz, J. S. Horwitz, P. Dorsey, R. Seed, and C. Vittoria, J. Appl. Phys. **71**, 5107 (1992).

⁶Y. Y. Song, S. Kalarickal, and C. E. Patton, J. Appl. Phys. **94**, 5103 (2003).

⁷S. D. Yoon and C. Vittoria, J. Appl. Phys. **96**, 2131 (2004).

⁸S. G. Wang, S. D. Yoon, and C. Vittoria, J. Appl. Phys. **92**, 6728 (2002).

⁹V. G. Harris, Z. Chen, Y. Chen, S. Yoon, T. Sakai, A. Gieler, A. Yang, Y. He, K. S. Ziemer, N. X. Sun, and C. Vittoria, J. Appl. Phys. **99**, 08M911 (2006).

¹⁰Y. Chen, T. Sakai, T. Chen, S. D. Yoon, A. L. Geiler, C. Vittoria, and V. G. Harris, Appl. Phys. Lett. **88**, 062516 (2006).

¹¹S. D. Yoon, C. Vittoria, and S. A. Oliver, J. Appl. Phys. **93**, 4023 (2003).

¹²S. D. Yoon and C. Vittoria, J. Appl. Phys. **93**, 8597 (2003).

Electric Field Tunable Low Loss Multiferroic Ferrimagnetic-ferroelectric Heterostructures**

By Jaydip Das,* Young-Yeal Song, Nan Mo, Pavol Krivosik, and Carl E. Patton

(Distribution version, accepted for publication in Advanced Materials, 12 December 2008)

Multiferroic materials have attracted major attention in recent years due to the unique possibility to tune the magnetic properties with a modest electric field and vice versa.^[1-3] Up to now, however, no single phase material has been put forward that demonstrates a practical capacity for such tuning at room temperature.^[4] This, in turn, has resulted in a shift in focus from single phase multiferroics to multiferroic heterostructures.^[5] Besides the new materials aspect of such structures, there are numerous device benefits. These include fast wide bandwidth tuning with low insertion loss in the microwave and millimeter wave frequency range, planar integrability, and negligible power consumption. These benefits speak to the strong potential for practical information storage, logic device, radar, satellite, and telecommunication applications.

Both multilayer thin film stacks as well as composite nanopillar films can be produced by various methods to satisfy such needs.^[6-8] The layer-by-layer fabrication of multilayer structures is generally more straightforward than the complicated growth process needed for nanopillar films. Previous workers have studied a variety of layered stacks with a broad range of ferromagnetic or ferrimagnetic (FM) and ferroelectric (FE)/piezoelectric (PE) components.^[9-13] Up to now, the main emphasis has been on FM-PE layers and the tuning of the magnetic response through the electric field induced stress on the FM layer. In our view, however, electric field tunable hybrid magneto-electric modes in the monolithic FM-FE structures can yield a better tuning of the magnetic response with electric fields and a better compatibility with various device applications.

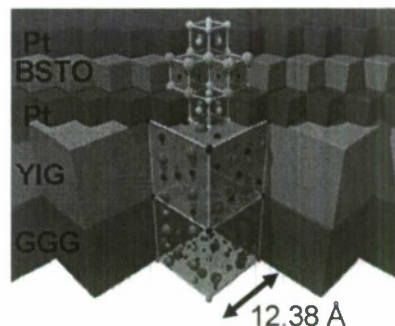
In principle, a micron thick FM-FE monolithic heterostructure, in combination with 10 nm or so embedded biasing electrodes, for example, can offer (1) a good quasi-lattice-to-lattice contact with the layers to give rise to the best possible magneto-electric coupling and (2) an appreciable magnetic tuning at small applied voltages in the range of 15-25 V or so. However, the challenge to fabricate heteroepitaxial ferrimagnetic oxide - metal electrode - ferroelectric oxide

stacks with the key physical properties of each layer properly maintained and with extremely smooth interfaces, has restricted the realization of such stacks so far. There have been some limited works with thick mechanically assembled structures that (1) does not offer the lattice-to-lattice contact between the layers and (2) needs about two orders of magnitude higher voltages than the monolithic structures.^[14, 15]

In this report, we present the realization of a significant tuning of magnetic response with extremely small applied voltages in a multiferroic FM-FE heterostructure. The structure was comprised of a pulsed laser deposited near single crystal yttrium iron garnet (YIG) layer with very low microwave loss, an oriented barium strontium titanate (BSTO) layer with good electric field tunable relative dielectric permittivity ϵ_r , and embedded platinum electrodes on a single crystal gadolinium gallium garnet (GGG) substrate. The results indicate an order of magnitude higher magneto-electric coupling than for pasted non-monolithic structures.

Scheme 1 shows a concept diagram of the cube-on-cube unit cell match-up for an all oriented YIG-Pt-BSTO-Pt-GGG stack. The cubic YIG lattice, with a lattice parameter of 12.38 Å, matches to the GGG lattice within 0.03%. This close match, along with the compatible oxygen coordinations, serves to promote epitaxial YIG film growth. The lattice parameter for platinum is about 3.93 Å. As apparent from the diagram, each YIG unit cell can reasonably accommodate nine face-centered-cubic (FCC) Pt unit cells with a mismatch of about 5%. Moving up the stack, the FCC BSTO lattice parameter is 3.95 Å, for a mismatch of about 0.5% with the Pt. All told, this overall assembly is expected to yield a reasonable heteroepitaxial layered structure. For ease of visualization, the concept diagram shown here is for (100) plane layers. Similar matchups apply to the actual structure developed here with (111) plane heteroepitaxy.

The initial YIG layer was deposited in a 100 mTorr oxygen atmosphere on the (111) GGG substrate heated to



Scheme 1. Concept diagram of the cube-on-cube unit cells of the YIG-Pt-BSTO-Pt heterostructure on the GGG substrate. Each box represents one unit cell of the respective material, as indicated. The atoms in the respective unit cells are also shown.

[*] Dr. J. Das, Dr. Y. Y. Song, Dr. N. Mo, Dr. P. Krivosik,

Prof. C. E. Patton
Department of Physics
Colorado State University
Fort Collins, Colorado 80523, USA
E-mail: jaydip@lamar.colostate.edu

Dr. P. Krivosik
Slovak University of Technology
81219 Bratislava, Slovakia

[**] This work was supported in part by the ARO-MURI, Grant W911NF-04-1-0247, the ONR, Grants N00014-07-1-0597 and N00014-08-1-1050 (through sub-award PT103701-SC101157 from Virginia Commonwealth University), and seed funding from the ARO- DARPA, Grant W911NF-06-1-0163.

about 800 °C. The thickness was held at a nominal value of about 0.3 μm . This is about as thick as one can go and still avoid a degradation in film quality and increase in microwave loss due to the lattice mismatch induced strain. This phase of the structure development is relatively straightforward. The challenge is to achieve near single crystal films with narrow ferromagnetic resonance (FMR) linewidths. The bare film, without the processing to obtain the additional layers, showed a 9.5 GHz derivative FMR linewidth of about 2 Oe. The processing needed to produce the subsequent layers provides some annealing of the YIG layer and a linewidth reduction to about 0.7 Oe.

The most critical step in the heteroepitaxial multilayer development lies in the BSTO and embedded Pt electrode layer growth on top of the YIG layer. The first step is to lay down a thin, epitaxial, continuous, and pinhole free Pt layer to serve as the seed for the oriented and continuous BSTO layer that comes next. The Pt layer must be thin, on the order of tens of nm, so that the hybrid YIG-BSTO mode tuning is not unduly compromised by the electrode in between. In order to realize an epitaxial Pt layer, high temperature processing is needed at, for example, 600 °C or so. However, the difference in the diffusion kinetics between oxides (YIG) and metals (the Pt) at such temperatures generally leads to an island like morphology that leaves the oxide surface partially exposed.^[16] This is especially problematic for the requisite thin Pt layers needed in this work. A special strategy was used here. The first step was to deposit a continuous but polycrystalline Pt layer with the GGG-YIG base structure/substrate held at room temperature. The subsequent high temperature BSTO

deposition step, considered in more detail below, provide an anneal for the platinum layer. This anneal produced the desired (111) oriented state. Note, however, that such a post deposition anneal can also lead to island formation. For this reason, it was necessary to lay down a fairly thick 30 nm layer of Pt in order to ensure a continuous, epitaxial, (111) oriented layer. This thickness is still about two orders of magnitude smaller than the platinum skin depth at 10 GHz, for example, so that the desired magneto-electric coupling between the YIG and the BSTO is not substantially affected.

Consider next the ferroelectric BSTO layer and the top Pt electrode capping layer. Two structures were prepared with nominal 1 and 5 μm thick BSTO layers. These layers were put down at 650 °C in 75 mTorr of oxygen. There was one caveat. Direct BSTO deposition on the oriented Pt gives rise to a polycrystalline layer with numerous cracks. In order to obtain a (111) crack free BSTO layer, a very thin nominal 5-10 nm MgO buffer layer was first deposited on the Pt. The 1 and 5 μm BSTO thickness choices were based on several trade-offs. (1) The thinner the layer, the less the applied voltage needed to get the same electric field across the FE layer. (2) Thin layers, however, also mean a reduced magneto-electric hybrid mode coupling between the FM and FE components. For the selected thicknesses, a 20 V BSTO layer tuning voltage corresponds to an electric field in the 10^6 V/m range. This should be sufficient to give strong magneto-electric coupling and reasonable tuning of the magnetic response.^[14] Finally, a 50 nm Pt layer was deposited on BSTO at room temperature to complete the YIG-Pt-BSTO-Pt structure.

X-ray diffraction (XRD), along with combined scanning electron microscopy (SEM) and energy dispersive spectroscopy (EDS) measurements, were used for the

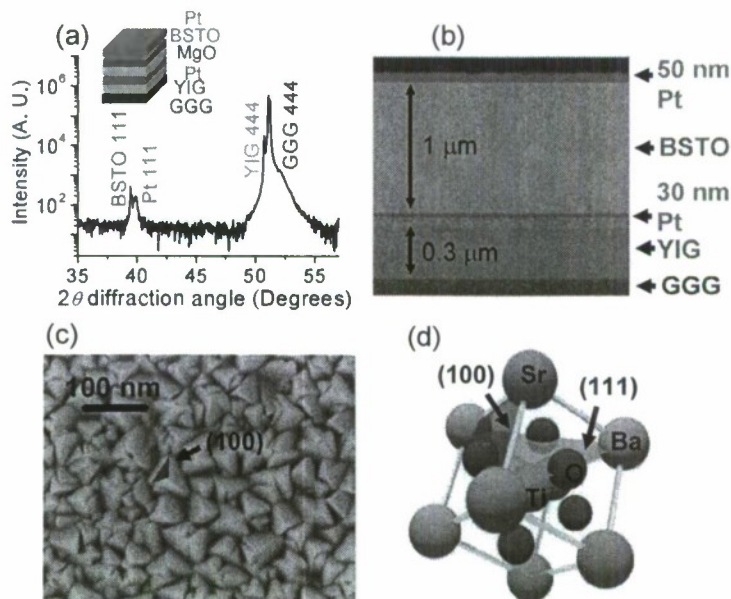


Figure 1. (a) X-ray diffraction 2θ scan for the heterostructure. (b) Element specific energy dispersive spectrum (EDS) results for the 0.3 μm thick YIG and the 1 μm thick BSTO layered structure with embedded Pt electrodes, as indicated. The data have been taken from the side. (c) Scanning electron micrograph (SEM) of the BSTO surface. The purple triangle marks one (100) facet. (d) Schematic BSTO unit cell diagram with the (111) plane (marked as grey) oriented horizontally, with one (100) facet marked with a purple triangle, as in (c).

structural, surface, and interface characterizations. Hysteresis loop and FMR measurements were used for the magnetic characterizations. Capacitance measurements were used to determine the relative permittivity ϵ_r and the voltage tunability of the BSTO. Finally, the FMR response and the tuning of this response were measured as a function of the applied BSTO layer bias voltage. The data indicate good (111) crystallographic orientation for all layers, a low FMR linewidth for the YIG, a high ϵ_r and good voltage tunability for the BSTO, and a strong magneto-electric hybrid mode coupling between the YIG and the BSTO layers.

Figure 1 shows representative XRD, EDS, and SEM results. Graph (a) shows the XRD pattern and schematic stacking diagram for the heterostructure. The origin of the various peaks are as labeled. One sees an intense YIG 444 peak that establishes the nearly ideal (111) orientation of the layer. The diagram also show weaker but distinct peaks associated with the epitaxial BSTO (111) and Pt (111) layers. The MgO is not discernable from the XRD data in (a) due to the extreme thinness (5-10 nm) of the layer. Thicker MgO layers (e.g., 100 nm) do show clear (111) XRD peaks.

Panel (b) shows the representative EDS mapping for the structure with the 1 μm thick BSTO layer, in a side view perspective. The thicknesses of visible YIG, Pt, and BSTO layers are as labeled. A composition analysis of the YIG and

BSTO layers confirms the expected atom fractions for both the materials. Panel (c) shows a SEM micrograph of the BSTO surface. One can see pyramidal shaped BSTO grains that point out of plane. For a given grain, one side of the pyramid corresponds to a (100) facet. One such facet is marked by a purple triangle in (c). Diagram (d) shows the schematic layout of the BSTO unit cell. One of the horizontal (111) planes is marked in grey. From this diagram, one can see clearly the pyramidal shape evident from the micrograph in (c) and the associated (100) facets. The SEM results, therefore, serve to confirm directly the (111) BSTO orientation given by the XRD data.

As mentioned earlier, the very good match between the YIG and GGG lattice is mainly responsible for the nearly single crystalline growth of the YIG layer along the (111) direction. The high melting point and high surface energy anisotropy then help to orient the embedded Pt layer along the most favorable (111) direction during the high temperature anneal that comes from the subsequent MgO and BSTO depositions.^[17] The (111) MgO buffer serves to promote the growth of (111) BSTO. Note that the BSTO layer, when deposited directly on the Pt layer, is polycrystalline in nature and shows cracks. This indicates a reasonable amount of strain on the BSTO from the 5% lattice mismatched YIG-Pt interface. Most likely, the 6% bigger MgO unit cell relative to

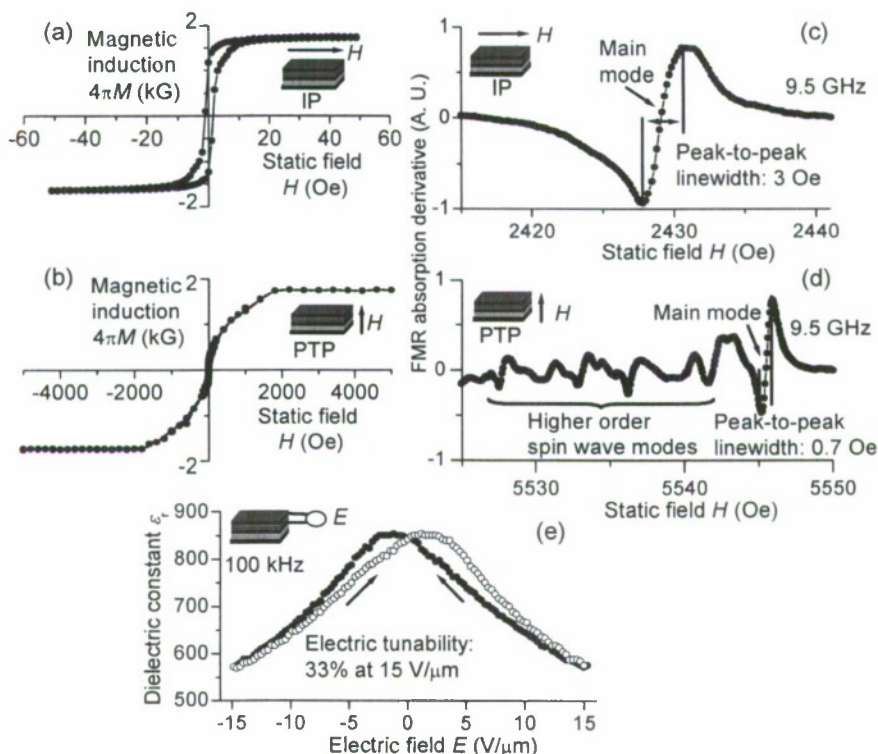


Figure 2. Magnetic and electric response results for the heterostructure. Hysteresis loop data for (a) in-plane (IP) and (b) perpendicular-to-plane (PTP) field orientations. Ferromagnetic resonance absorption derivative vs. static field H spectra at 9.5 GHz for (c) IP and (d) PTP field orientations. Labels designate the main mode and the higher order spin wave modes. (e) Dielectric constant ϵ_r vs. electric field E applied across the BSTO layer. The closed and open circles show the data for positive to negative and negative to positive field sweeps, as indicated.

the platinum, serves to compensate the YIG induced strain and allow for an oriented and crack-free BSTO layer. More extensive crystal chemistry related experiments coupled with theoretical analyses will be needed to obtain a better insight to the complicated nature of these oxide-metal-oxide interfaces.

Figure 2 shows representative room temperature hysteresis loop, FMR, and dielectric response results for the oriented heterostructure. Graphs (a) through (d) characterize the magnetic properties of the YIG layer. Graphs (a) and (b) show hysteresis loops in a magnetic induction $4\pi M$ vs. static field H format for in-plane (IP) and perpendicular-to-plane (PTP) static fields, respectively. Note the different field scales for the IP and PTP loop data. Graphs (c) and (d) show the 9.5 GHz IP and PTP field FMR responses, respectively, in a normalized absorption derivative vs. H format. The strongest peaks are labeled as the main mode in both graphs. The less intense peaks on the low field side of the spectra in graph (d) are labeled as higher order spin wave modes. Graph (e) shows the BSTO relative dielectric constant ϵ_r vs. the dc electric field E applied across the layer as obtained from the 100 kHz capacitance measurements.

Consider first the hysteresis loop data in (a) and (b). For the IP field case in (a), one sees a nearly square loop with a very low coercive force. The nominal saturation induction $4\pi M_s$ of about 1.7 kG is close to literature values for single crystal YIG.^[18] For the PTP field case in (b), the loop is definitely not square and saturation is realized only for fields above 1800 Oe or so, close to the saturation field expected for

an isotropic YIG film. This indicates that the YIG magnetization lies in the film plane, a state that is expected to yield the strongest magneto-electric coupling for the YIG-BSTO heterostructure.

Consider now the FMR results in (c) and (d). The relatively low and high main mode fields for the IP and PTP field configurations are consistent with the hysteresis loop properties in (a) and (b). The very narrow 0.7 Oe main mode derivative linewidth for the PTP field case in (d) is only slightly larger than the 0.5 Oe or so near-intrinsic linewidth found for bare YIG films. The presence of weak higher order spin wave modes at fields below the main mode gives additional evidence of the layer quality. The somewhat larger 3 Oe linewidth for the IP field case in (c) is likely due to a small contribution from the inhomogeneity related two magnon scattering in the YIG layer.

Finally, consider the electrical response properties of the BSTO layer in (e). Overall, one sees a significant tuning response for the relative dielectric permittivity ϵ_r with the electric field E . The fact that the response shows some small amount of hysteresis points to the ferroelectric nature of the BSTO layer. The cusp response and the nearly 35% change in ϵ_r at 15 V/ μm demonstrate the very good electric field tunability of the layer. The value of ϵ_r at $E \approx 0$ is close to literature values for the BSTO films.^[19] The important message from these data is that (1) the magnetic responses are consistent with the known properties of near perfect YIG single crystals, (2) the electric response shows the presence of a viable, high quality, high ϵ_r , and tunable BSTO layer, and (3) as such, the high quality YIG and BSTO layers realized here are expected to be amenable to a strong hybrid mode electric field tuning response.

Figure 3 shows the change in the magnetic response due to the application of electric fields for the heterostructure with the 5 μm BSTO layer. The main graph in (a) shows the 9.5 GHz IP field FMR profile in an absorption derivative vs. static magnetic field (H) format for applied voltages of zero and 25 V across the BSTO layer, as indicated. The inset shows the FMR resonance position vs. applied voltage V profile. Both sets of data are for increasing voltage. Graph (b) shows data in (a), but shown in terms of the incremental frequency shift in MHz/V as a function of voltage. The structure with the 1 μm BSTO layer showed no observable electric field driven FMR shift.

From graph (a), one sees that 25 V causes the FMR response to shift up in field by about 5 Oe. From the inset data, one sees a small down-shift to a shallow minimum at about 5 V followed by an incremental shift that increases rapidly with V . The incremental frequency response in graph (b) follows the same trend as in the inset of (a). The overall shape of this response is as one would expect for the hysteretic ferroelectric BSTO material.

The electric field tuning of the magnetic resonance revealed by the data in Fig. 3 is very substantial. Taken at face value, the 5 Oe FMR field shift in (a) amounts to an equivalent frequency shift of 14 MHz and the corresponding tunability is

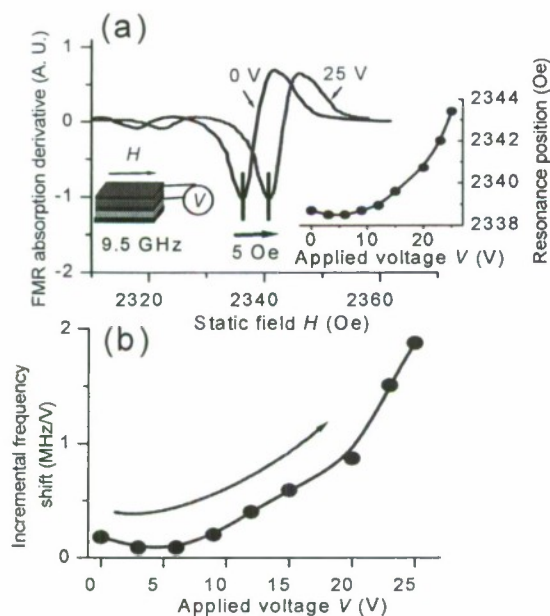


Figure 3. Electric field tuning of the magnetic response for the heterostructure. (a) The FMR absorption derivative vs. in-plane static field H spectra at 9.5 GHz for 0 and 25 V applied voltages, as indicated. Inset: The FMR resonance position as a function of the applied voltage V . (b) Incremental frequency shift vs. applied voltage. The circles show the data and the solid line is a guide to the eye.

about 0.6 MHz/V. This is about two times the hybrid mode tunability reported in Ref. [15] for mechanically pasted non-monolithic structures at a voltage of 400 V. The incremental frequency response in (b) shows an even higher tunability. As evident from the graph, the incremental frequency tuning is about 2 MHz/V at 25 V. This is nearly *one order of magnitude* greater than that reported previously.^[15] The good quasi-lattice-to-lattice contact is likely responsible for this enhanced tunability. This, in turn, is indicative of the very good magneto-electric coupling between the layers. Moreover, the 20 – 25 V bias voltages needed for the good coupling can be achieved easily in such multilayered structures.

There are two further points for consideration. First, for these monolithic structures as fabricated, at least some of the response in Fig. 3 may be due to stress tuning. Second, in the absence of a full theoretical analysis of the hybrid mode response, it is not yet clear whether the combined hybrid mode and stress tuning effects should add or subtract. A full theoretical understanding of these processes should allow for the full optimization of the tuning and realize an even higher tuning response than reported here. These considerations make the monolithic heterostructure approach extremely promising for electric field controlled small and fast magnetic devices. The ability to accomplish such control in planar monolithic structures, as demonstrated here, holds great promise for many practical applications in RF electronics, communications, electronic logic, and radar technology.

In summary, an electric field tunable magneto-electric monolithic multilayered heterostructure with ferrimagnetic and ferroelectric oxide layers, along with embedded metal electrodes, has been achieved. The "all oriented" heteroepitaxial stack shows the desirable physical properties of a ferrimagnetic layer with very low microwave loss and a ferroelectric layer with high permittivity and good electric field tunability. The structure shows a significant electric field tunability of the coupled hybrid magneto-electric modes for small applied voltages. This response is an order of magnitude better than previously obtained results for thick mechanically bonded layers.

The realization of such a hybridized structure is the first critical step in the fabrication of practical voltage tunable magnetic devices. Future work should focus on further increases in the tuning response through structure optimization and the use of multiple magnetic and electric layers. In the broad view, the materials advances realized here for the high temperature growth of high quality ferromagnetic oxide-metal-ferroelectric oxide stacks with very strong magneto-electric coupling is expected to have a significant impact on the physics, chemistry, and materials science of the thin film heterostructures.

[1] Y. N. Venevtsev, V. V. Gagulin, *Ferroelectrics* 1994, 162, 23.

[2] T. Kimura, T. Goto, H. Shintani, K. Ishizaka, T. Arima, Y. Tokura, *Nature* 2003, 426, 55.

- [3] J. Wang, J. B. Neaton, H. Zheng, V. Nagarajan, S. B. Ogale, B. Liu, D. Viehland, V. Vaithyanathan, D. G. Schlom, U. V. Waghmare, N. A. Spaldin, K. M. Rabe, M. Wuttig, R. Ramesh, *Science* 2003, 299, 1719.
- [4] S. -W. Cheong, M. Mostovoy, *Nature Mater.* 2007, 6, 13.
- [5] M. Fiebig, *J. Phys. D* 2005, 38, R123.
- [6] H. Zheng, J. Wang, S. E. Lofland, Z. Ma, L. Mohaddes-Ardabili, T. Zhao, L. Salamanca-Riba, S. R. Shinde, S. B. Ogale, F. Bai, D. Viehland, Y. Jia, D. G. Schlom, M. Wuttig, A. Roytburg, R. Ramesh, *Science* 2004, 303, 661.
- [7] R. Ramesh, N. A. Spaldin, *Nature Mater.* 2007, 6, 21.
- [8] W. J. Kim, W. Chang, S. B. Qadri, H. D. Wu, J. M. Pond, S. W. Kirchoefer, H. S. Newman, D. B. Chrisey, J. S. Horwitz, *Appl. Phys. A* 2000, 71, 7.
- [9] G. Srinivasan, E. T. Rasmussen, B. J. Levin, R. Hayes, *Phys. Rev. B* 2002, 65, 134402.
- [10] J. Ryu, S. Priya, K. Uchino, H. -E. Kim, *J. Electroceram.* 2002, 8, 107.
- [11] S. Dong, J. Cheng, J. F. Li, D. Viehland, *Appl. Phys. Lett.* 2003, 83, 4812.
- [12] J. Das, B. Kalinikos, A. Roy Barman, C. E. Patton, *Appl. Phys. Lett.* 2007, 91, 172516.
- [13] C. Pettiford, J. Lou, L. Russell, N. X. Sun, *Appl. Phys. Lett.* 2008, 92, 122506.
- [14] A. A. Semenov, S. F. Karmanenko, V. E. Demidov, B. A. Kalinikos, G. Srinivasan, A. N. Slavin, J. V. Mantese, *Appl. Phys. Lett.* 2006, 88, 033503.
- [15] A. B. Ustinov, V. S. Tiberkevich, G. Srinivasan, A. N. Slavin, A. Semenov, S. F. Karmanenko, B. A. Kalinikos, J. V. Mantese, R. Ramer, *J. Appl. Phys.* 2006, 100, 093905.
- [16] A. J. Francis, Y. Cao, P. A. Salvador, *Thin Solid Films* 2006, 496, 317.
- [17] D. Walton, *Phil. Mag.* 1962, 7, 1671.
- [18] W. H. von Autlock, *Handbook of Microwave Ferrite Materials*, Academic Press, London, 1965.
- [19] L. C. Sengupta, S. Sengupta, *IEEE Trans. Ultrason. Ferroelectr. Freq. Control* 1997, 44, 792.

Ferromagnetic resonance linewidth mechanisms in polycrystalline ferrites - the role of grain-to-grain and grain boundary two magnon scattering processes

Sangita Kalarickal,¹ Nan Mo,^{1,*} Pavol Krivosik^{1,2} and Carl E. Patton¹

¹*Department of Physics, Colorado State University, Fort Collins, Colorado 80523, U.S.A.*

²*Slovak University of Technology, 81219 Bratislava, Slovakia*

(Distribution version of manuscript for Phys. Rev. B, in press, BZ10690, 2009)

The frequency dependence of the ferromagnetic resonance linewidth ΔH in polycrystalline, hot isostatically pressed pure and Ca-Ge substituted yttrium iron garnet (YIG) spheres was measured between 1.95-6 GHz and analyzed. The linewidths for these ultradense ferrite materials are in the 5-40 Oe and 5-25 Oe ranges for the pure and the substituted YIG samples respectively. The ΔH vs. frequency data show especially sharp Buffler peaks due to the band edge crossover effect that is the signature for grain-to-grain (GG) two magnon scattering (TMS) [J. Appl Phys 30, 172S (1959)]. Both the GG and recent grain boundary (GB) TMS models were used to obtain quantitative fits to the data. The fits demonstrate the expected GG TMS contribution to the linewidth for frequencies above the Buffler peak. They also reveal two unexpected results, (1) a dominant GB TMS role for frequencies below the Buffler peak where the GG TMS linewidth contribution is essentially zero, and (2) a significant GB TMS role for frequencies above the peak where the linewidth has generally been associated with GG processes only. In the high frequency regime, the GB scattering term appears to explain about half of the overall linewidth.

PACS number(s): 76.50.+g, 75.30.Ds, 75.50.Gg,

I. INTRODUCTION

Despite many decades of study, the origins of microwave loss in polycrystalline magnetic materials remain a hot topic of research. There have been recent advances on several fronts, made possible in a large part by the availability of ultra dense ferrite samples with near zero porosity and second phase.^{1,2} The notable work of Nazarov and co-workers,³ for example, was the first to demonstrate that ultra dense polycrystalline ferrites can show close-to-theoretical linewidths based on grain-to-grain (GG) two magnon scattering (TMS).

More recent work of Mo and co-workers,⁴ in addition, has advanced the understanding of TMS relaxation processes in two ways. First, the application of clever metrology methods led to order of magnitude improvements in the accuracy of high field effective linewidth measurements. This has led, in turn, to the discovery of a new role for hybrid electromagnetic-exchange spin waves and new grain boundary (GB) two magnon scattering in polycrystalline ferrites. Second, and in a completely different context, even more recent ferromagnetic resonance (FMR) linewidth measurements in nano-crystalline metallic magnetic films have demonstrated the crucial roles of both

grain-to-grain and grain boundary two magnon scattering in microwave relaxation.^{5,6}

This work returns to the problem of microwave relaxation in ultra dense polycrystalline ferrites. The results from Ref. 3 have been extended to the low GHz regime and a comprehensive analysis of the full range of linewidth data over the characteristic Buffler peak⁷ in a linewidth vs. frequency data display format. This peak occurs for sphere samples when the FMR point moves above the top edge of the spin wave band at low wave numbers. For the yttrium iron garnet (YIG) materials used here, this effect occurs at about 3 GHz. The analysis shows that both GG and GB processes play important roles in the structure of this Buffler peak.

The paper is organized as follows. Section II gives a brief qualitative description of two magnon scattering processes in bulk ferrites and the qualitative origins of the Buffler peak. Section III elaborates sample properties, gives representative FMR profiles, and summarizes the overall linewidth vs. frequency results. Qualitative connections to two magnon scattering processes are also covered in this section. Section IV provides working equations for the quantitative analysis of the data. Section V presents theoretical fits to the data and makes specific

connections to the linewidth contributions due to different scattering processes. Section VI gives a summary and conclusion.

II. A VIGNETTE ON TWO MAGNON SCATTERING IN BULK FERRITES

The early FMR data for ferrite materials generally showed larger linewidths than expected for intrinsic processes. Theoretical considerations by Clogston *et al.*⁸ and Schlömann^{9,10} showed two possible origins of these large linewidths, TMS processes and simple inhomogeneous linebroadening. Inhomogeneity effects dominate when the corresponding local fields are large compared to the saturation induction $4\pi M_s$. Two magnon scattering, while still based on inhomogeneities, is more subtle. TMS processes rely on small local effective field spatial variations due to randomly oriented crystalline grain in anisotropic materials, dipole fields due to grain boundaries, second phase, pores, surface pits, magnetostriction, and so on. These field fluctuations lead to a coupling between the driven mode and available spin wave modes at the same frequency. The coupling provides an additional channel for energy relaxation from the driven mode, first to the degenerate spin waves, and eventually to the thermal bath. This is the essence of two magnon scattering.

The first experimental signature of two magnon scattering as a valid FMR relaxation process came from the seminal work of Buffler 1959.⁷ Schlömann's work, noted above, had pointed out a peculiar spin wave band effect for sphere shaped samples.⁹ As one increases the applied field, there is a point at which the FMR frequency crosses the top edge of the low wave number limit of the spin wave band. More specifically, the FMR point starts above this limit at low field and moves into the band only at high field. For YIG spheres, as an example, this band edge crossover point occurs in the 3.5 GHz range, depending on the actual saturation induction of the material.

Even today, many FMR experts do not know about this basic effect, even though it provides the historical experimental key to two magnon scattering relaxation. One possible reason is that the predominant FMR work in recent years has been for thin films. This band edge crossover effect occurs only for spheres and not for any of the other basic geometries of interest.

The experimental manifestation of this effect is an abrupt increase in the linewidth as the FMR frequency moves through the crossover frequency, taken here as f_x . This is then followed by a slow decrease in the linewidth at higher frequencies. This is a purely geometric effect. It occurs for spheres, but not for other sample shapes. C. R.

Buffler was the first to observe this effect experimentally.⁷ This direct early experimental evidence for TMS processes provided the key data that pointed the way to further theory and experiments on anisotropy, porosity, and surface pit TMS processes.¹¹ As noted in the introduction, new results continue to emerge. Mo and co-workers have shown,⁶ for example, that grain boundary TMS processes related to very short wavelength spin waves must be added to the above list of interactions for a complete picture of this important mechanism.

Figure 1 illustrates the band edge crossover effect described above. The (a), (b), and (c) graphs show spin wave band diagrams of normalized spin wave frequency vs. wave number k for three different fields for sphere shaped YIG samples, as indicated. Graph (b) corresponds to the FMR band edge crossover. The specific field/frequency operating points were chosen to demonstrate this effect. The dashed horizontal line shows the degenerate mode cut across the bands at the FMR frequency for these three cases. The vertical shaded region across the low k edge of the band for $k < k_a = 1 \times 10^4$ rad/cm accentuates those modes that can give a strong GG TMS contribution for YIG grain sizes in the 10 μm range. The connection between k_a , grain size, and TMS processes will be elaborated shortly.

Figure 1 is intended to convey two main points. First, as one increases the external field, the well known upward shift in spin wave band and the FMR frequency is accompanied by a crossover of the FMR frequency from outside the low k part of the band at low field to completely inside the band at high field. The crossover frequency f_x is equal to $(2/3)(|\gamma|/2\pi)4\pi M_s$, where γ denotes the electron gyromagnetic ratio. With $4\pi M_s$ taken at the nominal YIG value of 1750 G and $|\gamma|/2\pi$ taken at the nominal free electron value of 2.8 GHz/kG, this crossover effect occurs at about 3.3 GHz. The specific diagrams in Fig. 1 have been selected to underscore this basic effect. It is a little known effect, even though it was crucial to the initial realization of the role of TMS processes in microwave ferrite relaxation.

The second point concerns the interplay between the actual coupling to the degenerate modes and the crossover effect that leads to the TMS signature in the linewidth vs. frequency profile discovered by Buffler. In this context, the key is in the shaded vertical strip of modes at the extreme low k side for each of the spin wave band diagrams in Fig. 1. This strip corresponds to the modes that are strongly coupled to the FMR mode for coarse grain ferrites. Here, "coarse grain" is taken to denote grain sizes in the range of tens of micrometers that are typical for polycrystalline ferrites made by standard sintering or hot pressing methods.

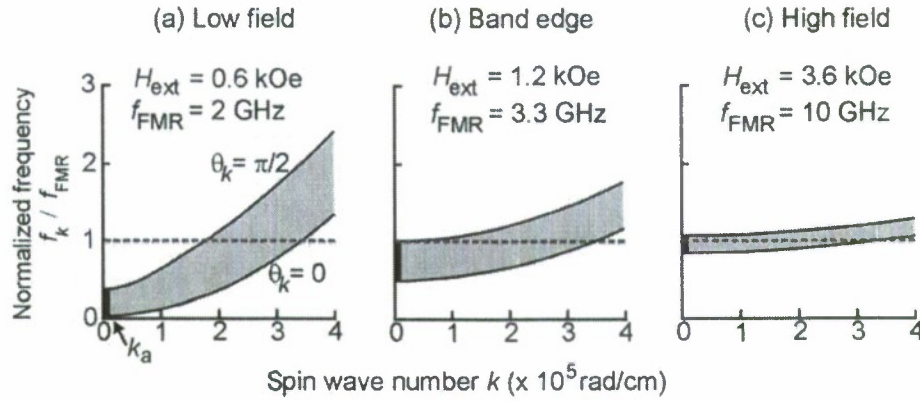


FIG 1.(Color online) Schematic spin wave band diagrams of spin wave frequency f_k , normalized to the ferromagnetic resonance frequency (FMR) f_{FMR} , as a function of the spin wave number k for sphere shaped samples. Graphs (a), (b), and (c) are for external applied static field (H_{ext}) values of 0.6, 1.2 and 3.6 kOe and the corresponding FMR frequency values, as indicated. Graph (b) corresponds to the band edge crossover point at $f_{\text{FMR}} = f_x$. The curves are for yttrium iron garnet magnetic parameters. The curved lines show the band limits for spin wave propagation angles (θ_k) relative to the field direction of zero and $\pi/2$, as indicated. The shaded regions indicate the full band. The horizontal dashed lines show the cut across the band at the FMR frequency for $f_k / f_{\text{FMR}} = 1$. The arrow at $k_a \sim 1 \times 10^4$ rad/cm and narrow vertical shaded regions for $k < k_a$ denote the region of strong two magnon grain-to-grain scattering for a nominal grain size of 10 μm .

Generally, two magnon scattering has a strong coupling between the driven FMR mode for $k \approx 0$ to degenerate spin wave modes with $k < k_a \approx 1/a$ or so, where a is the grain size. For $a \sim 10 \mu\text{m}$, one has $k_a \approx 10^4$ rad/cm. One can see that as the field is increased and the FMR frequency moves from above the band edge point to inside the band, the low k modes available for strong scattering come into play quite abruptly. The fact that the density of states for the degenerate spin wave modes is also quite large at the top edge of the spin wave band leads to a pronounced peak in the linewidth as one moves through the crossover frequency. The quantitative connection between the linewidth vs. frequency data and the TMS analysis for GG scattering will be covered in Section IV. Additionally, the results will also reveal a new effect, namely, a nonzero GB scattering to high k spin wave modes. This effect shows up most clearly for frequencies in the band regime of graph (a) in Fig. 1. One can see that for GG scattering alone, the TMS linewidth in this regime is zero because there are no degenerate low k modes.

III. SAMPLES AND MEASUREMENTS

The YIG samples were made by standard hot isostatic pressing (Hipping) ceramic methods. Nazarov *et al.* have provided the fabrication details.³ These authors also provided X-band FMR linewidth data that establish the density of the materials to be near theoretical. The residual

porosity was less than 1% and the half power 10 GHz FMR linewidth was 13 Oe. The average grain size was 8 μm . Spheres were fabricated from the interior regions of the hipped blocks, to avoid possible problems with oxygen deficient surface regions. A similar procedure was also applied to Ca-Ge substituted YIG. The specific results in this chapter, shown for nominal 2 mm diameter spheres, confirm the nearly complete elimination of porosity for the hipped materials.

The FMR profiles were measured at frequencies between 1.95 and 6 GHz with a broadband strip transmission line FMR spectrometer described in Ref. [12]. Figure 2 shows representative data. The graph shows a sequence of profiles of the FMR absorption derivative vs. static external field H_{ext} for selected frequencies, as indicated. One sees the expected shift in the FMR fields with increasing frequency. Note that the profile is somewhat narrow at 1.9 GHz, becomes very narrow at 3 GHz, broadens substantially at 4.0 GHz, and then appears to narrow somewhat at 5.3 GHz. The behavior from 3 to 5.3 GHz is a direct consequence of the band edge crossover GG TMS effect from Sec. II. The substantial jump in linewidth from 3 to 4 GHz is a direct result of this crossover. The fall-off from 4 to 5.3 GHz is due to a gradual drop in the available degenerate spin wave states for scattering. The relatively broad line at 1.9 GHz is due to the unsaturated state of the sample at these fields.

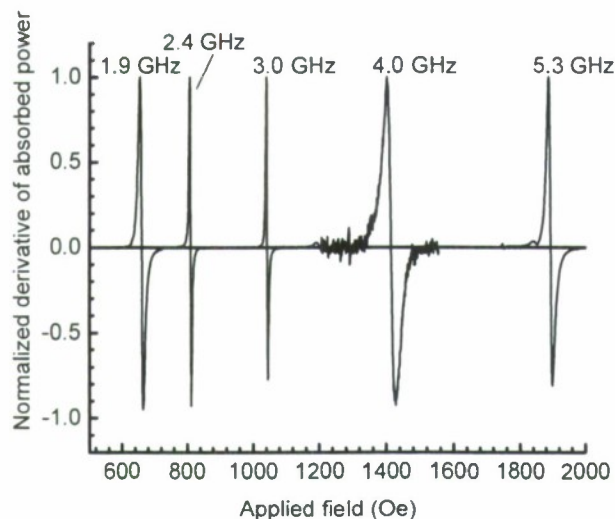


FIG. 2. Normalized ferromagnetic resonance (FMR) absorption derivative vs. field profiles for the hipped YIG sphere at selected FMR pump frequencies, as indicated.

Data of the sort shown in Fig. 2 were also used to establish the gyromagnetic ratio γ . The FMR frequency f_{FMR} for sphere shaped samples is equal to $(|\gamma|/2\pi)H$. The data on FMR frequency vs. field yielded a $|\gamma|/2\pi$ value of 2.765 MHz/Oe. This paper will use Gaussian units for the working equations for the data analysis, as needed, and for the theoretical development. Note also that the “ f ” notation will denote frequency in Hz or related units. In the theoretical discussions to follow, it will also be appropriate to bring in the usual “ ω ” notation for angular frequency in rad/s.

Linewidth values were obtained from FMR derivative profiles similar to those shown in Fig. 2, but for a fine grid of frequency points from 2 to 6 GHz. For each profile, the half power field swept linewidth ΔH was taken as the difference in field values at the extrema of the derivative profile multiplied by $\sqrt{3}$. This connection is strictly applicable to Lorentzian absorption profiles. Integrated absorption profiles were, in fact, near Lorentzian.

Figure 3 shows representative ΔH vs. f_{FMR} results. These particular data, as in Fig. 2, are for the hipped YIG sphere. The main portion of the data is shown by solid symbols. These data will be the focus of the two magnon analysis to follow. The portion of the data for $f_{\text{FMR}} < 3$ GHz or so are shown by blue open circles. These data show a gradual upturn below 3 GHz and a more rapid increase below about 2.2 GHz. This response is related to demagnetization and low field loss effects and is not of direct interest here. The vertical dashed line at $f_{\text{FMR}} \approx 3.6$ GHz marks the band edge crossover frequency. This point is shifted from the 3.3 GHz value shown in Fig. 1 because of the larger nominal $4\pi M_s$ value of 1950 G for the hipped YIG material, as obtained from fits to be considered shortly. The schematic low field and high field region spin wave

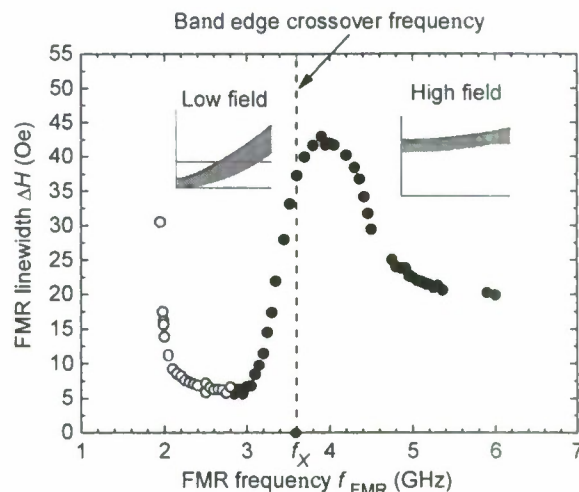


FIG. 3 (Color online) Ferromagnetic resonance (FMR) linewidth ΔH as a function of the FMR frequency f_{FMR} for the hipped YIG sphere. The open blue symbols show data for the low field regime for which the sample is not saturated. The vertical dashed line marks the calculated band edge crossover frequency f_X . The insets show schematic spin wave frequency vs. wave number diagrams for the low field below crossover ($f < f_X$) and high field above crossover $f > f_X$ regimes.

band diagrams for the regions below and above the crossover point track the (a) and (c) diagrams from Fig. 1.

The solid circle data in Fig. 3 demonstrate the two magnon band edge crossover effect discussed in Sec. II. There is a rapid increase in linewidth as one approaches the crossover frequency from below, followed by a distinct peak and a gradual leveling off at high frequency. It is notable that there is sizeable linewidth increase even for frequencies below the crossover frequency. The coarse grain scattering scenario from Sec. II and the exclusive two magnon coupling to extremely low k modes alone would give a sharp cutoff at the crossover frequency f_X rather than the response shown by the data. As will be discussed shortly, the two magnon linewidth “leakage” into the frequency regime below f_X is a direct result of grain boundary TMS processes. It also turns out that GB scattering also plays a significant role in the frequency regime above crossover. This is alluded to in the last part of the discussion of Fig. 1 at the end of Sec. II. These points will be made quantitative in Secs. IV and V.

IV TWO MAGNON SCATTERING RELAXATION AND LINEWIDTH CONNECTIONS

As noted in Section II, there is extensive literature on the two magnon scattering relaxation theory in magnetic systems in general.^{8-11,13-15} Reference 4 casts the general two magnon scattering relaxation rate in the form

$$\eta_{\text{TMS}} = \frac{\omega_M^2}{8\pi^3} \int_{\mathbf{k}\text{-space}} \delta(\omega - \omega_k) C(\mathbf{k}) \Lambda(\mathbf{k}, \omega) d\mathbf{k}. \quad (1)$$

The parameter $\omega_M = |\gamma| 4\pi M_s$ expresses the saturation induction in frequency units. The delta function $\delta(\omega - \omega_k)$ constrains the scattering to degenerate spin wave modes with a frequency ω_k equal to the pump frequency ω . The $C(\mathbf{k})$ factor defines the coupling strength between the uniform mode and particular degenerate spin wave modes at some wave vector \mathbf{k} . The $\Lambda(\mathbf{k}, \omega)$ factor accounts for the ellipticity of the spin wave mode. For sphere shaped samples, the connection between η_{TMS} and ΔH amounts to a simple conversion, according to $\Delta H = 2\eta_{\text{TMS}} / |\gamma|$.

As discussed in earlier sections, two distinct TMS processes turn out to be important for polycrystalline ferrites, one related to GG scattering and to GB scattering. These processes can be taken to occur in parallel. In order to deal with the differences in the k -dependences of the coupling terms for the two processes, it proves useful to write Eq. (1) in a slightly different form. Keep in mind that for GG scattering, it is the grain size a that controls the scattering and the coupling is to low wave number modes with $k < k_a$ alone. Recall the discussion related to Fig. 1 and coarse grain scattering. For GB scattering, it is the much narrower sub-micron size grain boundary that controls the scattering. This process is definitely not coarse grain scattering but extends out to much larger k -values.

A useful starting point for the separation of the different k -dependences for GG and GB scattering is to recast the formal \mathbf{k} -space integral in Eq. (1) in terms of the specific integrals over wave number k and the polar and azimuthal spin wave propagation angles θ_k and ϕ_k , respectively.

$$\eta_{\text{TMS}} = \frac{\omega_M^2}{8\pi^3} \int_0^\infty dk \int_0^\pi d\cos\theta_k \int_0^{2\pi} d\phi_k [F(\mathbf{k}) \Lambda(\mathbf{k}, \omega) \delta(\omega - \omega_k)]. \quad (2)$$

The function $F(\mathbf{k}) = 4\pi k^2 C(\mathbf{k})$ folds in the numerical 4π factor from the angular integrals and the explicit k^2 factor from the k -integral into the new form of the coupling. As the discussion below will demonstrate, the $F(\mathbf{k})$ form makes it possible to gain an intuitive understanding of the GG and GB contributions to the scattering.

First consider the working equations for GG scattering. In this case, one can write $F(\mathbf{k})$ in the form

$$F_{\text{GG}}(\mathbf{k}) = F_{\text{GG}}(k) = \frac{8\pi^4}{105} \left(\frac{H_A}{4\pi M_s} \right)^2 g(k). \quad (3)$$

The new $g(k)$ function is used here to separate out the k -dependent part of the degenerate spin wave coupling for GG scattering. This factor is taken in the form first used by Schlömann⁹ and recently re-derived by hamiltonian methods by Krivosik *et al.* in Ref. 14

$$g(k) = \frac{4}{\pi} \frac{k^2 a^3}{(1 + k^2 a^2)^2}. \quad (4)$$

In the above, H_A denotes an effective cubic anisotropy field $2K_1/M_s$, where K_1 is the first order cubic magnetocrystalline anisotropy energy constant. In the qualitative discussion above, a was taken as the grain size. In a more general sense, a may be taken as a mean inhomogeneity size. One can see that the $g(k)$ function peaks at $k = k_a = 1/a$. Recall, however, that the k^2 factor in the numerator derives from the same factor in the k -space differential volume $4\pi k^2 dk$. Without this factor, the $g(k)$ corresponds to the Fourier transform of a fluctuating field with a correlation length equal to the mean grain size.

The spin wave ellipticity factor for GG scattering, labeled here as $\Lambda_{\text{GG}}(\mathbf{k}, \omega)$ was also developed first by Schlömann in Ref. 9 and is written here as

$$\Lambda_{\text{GG}}(\mathbf{k}, \omega) = 1 + 19 \frac{A(\mathbf{k}, H)}{\omega}, \quad (5)$$

where

$$A(\mathbf{k}, H) = |\gamma| H_i + |\gamma| D k^2 + 2\pi M_s \sin^2 \theta_k. \quad (6)$$

The internal field H_i in Eq. (6) is equal to $H - (4\pi M_s/3)$ for sphere shaped samples. The D parameter takes exchange into account. The nominal D -value for YIG materials is 5.2×10^{-9} Oe cm^{2.4}. The numerical factors in Eqs (3) and (5) follow the Schlömann form. They are a result of a systematic averaging over the randomly oriented cubic crystallites for the YIG system. Further details on the averaging mechanics are given by McMichael and Krivosik in Ref. 13.

For GB scattering, the $F(\mathbf{k})$ and $\Lambda(\mathbf{k}, \omega)$ functions take a somewhat different form. The full theory is summarized in Refs. 4 and 6, and developed in detail in Ref. 15. The coupling and polarization terms are different from those for the grain-grain anisotropy based scattering. The formulae given below follow the nomenclature of Ref. 4. The $F(\mathbf{k})$ for GB scattering now takes the form

$$F_{GB}(\mathbf{k}) = F_{GB}(k) = 12\pi^4 l_{gb}^2 k^2 g(k). \quad (7)$$

Following Ref. 4, l_{gb} denotes an effective grain boundary thickness parameter. From physical considerations, l_{gb} scales with the ratio of surface anisotropy energy to the magnetostatic self energy and is on order of tens of nanometers for polycrystalline ferrites. Fits to the data in the next section will yield nominal values of 9 nm for the pure YIG and 16 nm for the Ca-Ge substituted YIG samples. Note the additional k^2 factor in the GB coupling. With this modification, the k -dependence of the scattering defined through $k^2 f(k)$ sees major modifications. Now the scattering is essentially zero for $k \ll k_a$, begins to grow for $k \approx k_a$, and levels off to some maximum value for $k \gg k_a$. This is precisely the response expected for GB scattering. One can now have strong coupling to very short wavelength spin waves in the extremely high k part of the spin wave manifold.

Also following Ref. 4, the $\Lambda(\mathbf{k}, \omega)$ spin wave polarization term for GB scattering is now written as

$$\Lambda_{GB}(\mathbf{k}, \omega) = 1 + \frac{A(\mathbf{k}, H)}{\omega}. \quad (8)$$

The different numerical factors in Eqs. (6) and (8) arise from the different symmetries in the GG and GB scattering problems. As noted above, GG scattering involves an averaging over the grains in the 3D system. For GB scattering, in contrast, one is dealing with an interface effect that is treated in a simplified 2D model.¹⁵

Figure 4 shows the same bulk spin wave band diagrams of frequency f_k vs. wave number k as given in graphs (a) and (c) of Fig. 1, except that the k -axis is given in logarithmic scale. Also as in Fig. 1, horizontal dashed red lines are used to show k -range of the degenerate mode at the indicated FMR frequency in each case. The solid blue and dashed green curves in both graphs show plots of the $F(k)$ functions developed above for GG and GB scattering, respectively. The curves are normalized to maximum values and denoted as $F^{\text{norm}}(k)$. Recall that the peak GG coupling occurs for $k = k_a = 1/a$. The GB coupling shows no peak, but simply levels off at its maximum value at very high k -values.

The overall point of Fig. 4 is to demonstrate the very different coupling conditions for fields below the band edge, as in (a), and fields above the band edge, as in (b). For the below-the-band-edge situation in (a), one can see that the degenerate mode line cuts the spin wave band in the range of very high k values for which the GB coupling is strong and that there are no degenerate low k modes. This means that the two magnon processes are limited to GB

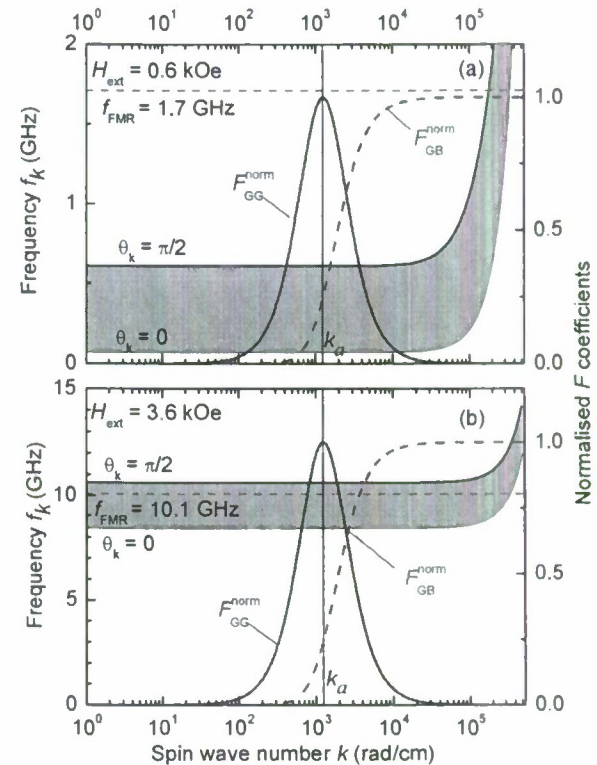


FIG 4. (Color online) Each graph shows (i) spin wave frequency f_k vs. wave number k for a sphere shaped yttrium iron garnet sample with materials parameters that match the experiment and (ii) the normalized two magnon scattering coupling coefficient F^{norm} vs. k for grain-to-grain (GG) and grain boundary (GB) two magnon scattering (TMS), as indicated. The curves in (a) and (b) were obtained with external field H_{ext} -values of 0.6 and 3.6 kOe, respectively. The spin wave band nomenclature and labels are the same as for Fig. 1. The solid vertical line at $k = k_a = 1/a = 1.25 \times 10^3$ rad/cm, where a is the nominal grain size, marks the transition k -value for both TMS processes.

scattering. As will be shown shortly, GB scattering turns out to provide a reasonable quantitative model for the observed linewidth tail for frequencies below the band edge crossover frequency f_X .

Contrast this with the situation in Fig 4 (b). Here one can see that the degenerate mode line cuts the spin wave band over the full range of wave number k values from the low limit at $k \approx 0$ out to the very high values at the edge of the spin wave band for $k \approx 10^5 - 10^6$ rad/cm. These degenerate modes now span regions of k -space for which the $F(k)$ functions for *both* GG and GB scattering indicate strong coupling. The quantitative fits of the theory to the data given below will show that both processes contribute substantially to the two magnon linewidth for frequencies above the band edge crossover frequency f_X .

V LINEWIDTH ANALYSIS

Graphs (a) and (b) in Fig. 5 show, respectively, the full ensemble of linewidth vs. frequency data for both the pure YIG and substituted YIG samples. The open circles in (a) show the same data as in Fig. 3. The solid circles show extended frequency data from Ref. 3. The error bars for all data points are in the range of ± 0.5 Oe. The panels also show theoretical fits based on a simple model of GG and GB TMS processes that operate in parallel. The fits do not include either a Landau-Lifshitz linewidth term or inhomogeneity broadening effects. The various curves show computed results for GG scattering, GB scattering, and the sum of these two processes, as indicated. The theoretical curves were obtained for a common grain size a of $8 \mu\text{m}$, and with $4\pi M_s$, H_A , l_{gb} , and $|\gamma|/2\pi$ values of 1952 G, 40 Oe, 9 nm, and 2.765 MHz/Oe, respectively, for the pure YIG and 990 G, 20 Oe, 16.2 nm, and 2.76 MHz/Oe, respectively, for the substituted YIG. These materials parameters are consistent with the ferrite literature.^{17,18} The critical fit parameters were H_A and l_{gb} . Following Ref. 4, an effective grain boundary thickness parameter l_{gb} in the nm range is also reasonable for the hipped ferrite microstructure.

Both graphs show very prominent Buffler peaks. In line with the extended discussion in Sec. III, these peaks provide the basic signature of GG scattering. The prominence of the Buffler peaks is due to the use of hipped samples with near theoretical density. Porosity effects in the original Buffler samples resulted in significantly larger linewidths

and a broader peak. Overall, the linewidths in (b) for sample B are even lower than those in (a) because of the use of Ca-Ge substituted YIG materials with a lower anisotropy. The GG based two magnon scattering scales with the anisotropy.^{16,17}

The physical origins of the linewidth vs. frequency response manifested by the low frequency data in (a) was discussed in connection with Fig. 3. From Fig. 5, one sees that both samples show essentially the same response. Each data set shows (1) a rapid increase in linewidth at very low frequencies due to sample demagnetization, (2) a local minimum with a nonzero linewidth at frequencies just below the Buffler peak, (3) a rapid increase that forms the Buffler peak as one moves through the band edge crossover, and (4) a gradual decrease in linewidth as one moves to frequencies well above the Buffler peak. These effects occur for somewhat lower frequencies in (b) due to the reduced magnetization for the Ca-Ge-YIG.

The new points to be considered here, relative to Fig. 3, concern the actual fits to the data from the combined GG and GB TMS models. These fits tell the quantitative story of the TMS processes outlined in general terms in Secs. III and IV. The fits demonstrate three points. First, it is clear that one can realize a remarkably good fit to the data for two different materials based on TMS processes. The fact that the theoretical curves show a divergence at the band edge crossover frequency is of no consequence here. This divergence is due to the neglect of the nonzero relaxation rate for the product spin waves from the TMS processes. Schlömann⁹ has shown that the inclusion of a nonzero spin

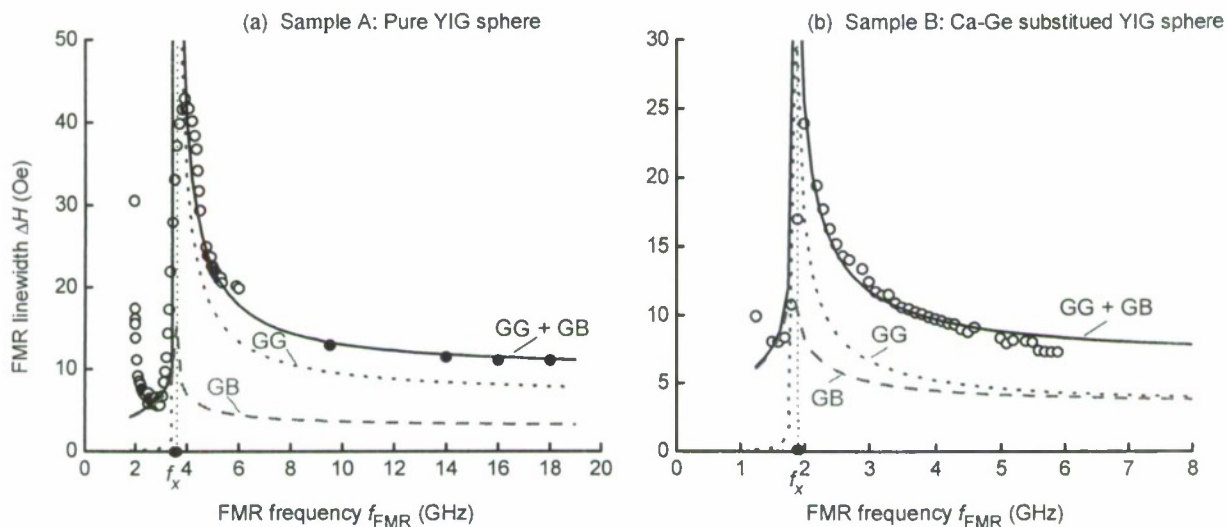


FIG. 5 (Color online) Graphs (a) and (b) show the ferromagnetic resonance (FMR) linewidth ΔH as a function of the FMR frequency f_{FMR} for sphere shaped samples of hipped yttrium iron garnet (YIG) and Ca-Ge substituted YIG, respectively. The open circles show data from the broadband strip transmission line measurements. The solid circles in (a) show data on the same sample from Nazarov *et al.*³ The dashed and dotted curves show fitted ΔH vs. f_{FMR} results from model calculations for grain boundary (GB) and grain-to-grain (GG) two magnon scattering processes, respectively. The solid curves show the sum of the GB and GG results.

waves linewidth in TMS calculations eliminate such divergences. One obtains, thereby, theoretical curves that match effective linewidth data quite nicely, for example.¹⁸

Second, the GB TMS linewidth fits for the frequency region just below the Buffler peak band confirm the expectation from Sec. IV that grain boundary scattering processes must play a role in this region. In fact, the theoretical response also matches this portion of the data quite nicely.

The third point comprises a somewhat unexpected result. The realization of data over a wide range of frequencies on both sides of the Buffler peak, in combination with calculations based on a two component GG/GB TMS process; show that *both* processes make significant contributions to the linewidth. The fits in Ref. 3 were done for GG scattering alone and appeared to match the data. The problem in this reference, however, was in the availability of limited high frequency data only and no experimental points close to or below the Buffler peak. In the present work, it is these low frequency data points that provide the clue to the role of GB scattering. Once the required GB scattering parameters are included to fit the data for $f < f_x$, a necessary GB contribution propagates into the $f > f_x$ frequency regime. The fits show that in the $f > f_x$ region, one has roughly equal GG and GB two magnon scattering contributions to the linewidth.

With two magnon processes properly taken into account, it is entirely reasonable to ignore any possible intrinsic linewidth terms in doing the fits shown in Fig. 5. Effective linewidth measurements have shown that such contributions are below one Oersted over the frequency range shown here.¹⁹

VI SUMMARY AND CONCLUSION

The early linewidth results for polycrystalline ferrites in the region of the Buffler peak provided the initial evidence for the role of two magnon scattering relaxation in ferromagnetic resonance. These classic results have been now extended and made quantitative, and several new aspects of TMS relaxation in polycrystalline ferrites have been revealed. The new data on ultradense pure and substituted YIG materials with nominal 10 micron grain sizes show an especially sharp Buffler peak that derives from the band edge crossover effect initially reported in Ref. 7. Due in part to recent new developments in two magnon relaxation models for both grain-to-grain anisotropy scattering (GG scattering) and grain boundary (GB) scattering, it has been possible to obtain quantitative TMS fits to the data. These fits demonstrate the expected role of GG scattering in the relaxation, just as suggested by Buffler. The fits also reveal the somewhat unexpected role of GB scattering as a contributor to the TMS linewidth in

polycrystalline ferrites. (1) It is found that GB scattering plays a role in the frequency regime below the Buffler peak where simple two magnon low- k scattering models give no TMS contribution. The nominal GB TMS linewidth in this regime is about 5 Oe. (2) It is also found that GB scattering contributes about half of the overall TMS linewidth in the frequency regime above the peak where GG scattering was previously thought to be dominant.

ACKNOWLEDGEMENTS

This work was sponsored in part by the Office of Naval Research Grant Nos. N00014-07-1-0597 and N00014-08-1-1050 (subgrant from Virginia Commonwealth University), U.S. Army Research Office Grant No. W911NF-04-1-0247 (MURI), the Information Storage Industry Consortium extremely high density recording program, and Seagate Technology. The hipped pure YIG sample was kindly provided through a collaboration with G. M. Argentina (Pacific Ceramics, Inc.) and J. J. Green and H. J. Van Hook (private consultants, Lexington, Massachusetts). The hipped substituted YIG sample was kindly provided by TCI Ceramics, Bethlehem, Pennsylvania.

Footnote:

*: ² Now at CIS, Tyco Electronics, Reno Nevada 89521, U.S.A.

REFERENCES

- ¹H. J. Van Hook and C. B. Willingham, *Adv. Ceram.* **15**, 1637 (1984).
- ²H. V. Atkinson and S. D. A, *Metall. Mater. Trans. A* **31A**, 2981 (2000).
- ³A. V. Nazarov, D. Menard, J. J. Green, C. E. Patton, G. M. Argentina, and H. J. Van Hook, *J. Appl. Phys.* **94**, 7227 (2003).
- ⁴N. Mo, J. J. Green, P. Krivosik, and C. E. Patton, *J. Appl. Phys.* **101**, 023914 (2007).
- ⁵S. S. Kalarickal, P. Krivosik, J. Das, K. S. Kim, and C. E. Patton, *Phys. Rev. B* **77**, 054427 (2008).
- ⁶N. Mo, J. Hohlfeld, M. u. Islam, C. S. Brown, E. Girt, P. Krivosik, W. Tong, A. Rebei, and C. E. Patton, *Appl. Phys. Lett.* **92**, 022506 (2008).
- ⁷C. R. Buffler, *J. Appl. Phys.* **30**, 172S (1959).
- ⁸A. M. Clogston, H. Suhl, L. R. Walker, and P. W. Anderson, *J. Phys. Chem. Solids* **1**, 129 (1956).
- ⁹E. Schloemann, *J. Phys. Chem. Solids* **6**, 242 (1958).
- ¹⁰E. Schloemann, *Phys. Rev.* **182**, 632 (1969).
- ¹¹M. Sparks, *Ferromagnetic Relaxation Theory* (McGraw-Hill, New York, 1964).
- ¹²S. S. Kalarickal, P. Krivosik, M. Wu, C. E. Patton, M. L. Schneider, P. Kabos, T. J. Silva, and J. P. Nibarger, *J. Appl. Phys.* **99**, 093909 (2006).

- ¹³R. D. McMichael and P. Krivosik, IEEE Trans. Magn. **40**, 2 (2004).
- ¹⁴P. Krivosik, N. Mo, S. S. Kalarickal, and C. E. Patton, J. Appl Phys **101**, 083901 (2007).
- ¹⁵N. Mo, Ph.D. thesis, Colorado State University, 2006.
- ¹⁶H. J. Van Hook, J. J. Green, F. Euler, and E. R. Czerlinsky, J. Appl Phys **39**, 730 (1968).
- ¹⁷C. E. Patton and H. J. Van Hook, J. Appl. Phys **43**, 2872 (1972).
- ¹⁸C. E. Patton, Phys. Rev. **179**, 352 (1969).
- ¹⁹N. Mo, Y. Y. Song, C. E. Patton, J. Appl. Phys. **97**, 093901 (2005)

Three-magnon splitting and confluence processes for spin-wave excitations in yttrium iron garnet films - Wave vector selective Brillouin light scattering measurements and analysis.

César L. Ordóñez-Romero,^{1,2} Boris A. Kalinikos,^{1,3} Pavol Krivosik,^{1,4} Wei Tong,¹ Pavel Kabos,⁵ and Carl E. Patton¹

¹ *Department of Physics, Colorado State University, Fort Collins, Colorado, USA*

² *Universidad Nacional Autónoma de México, Ciudad Universitaria, México D.F., México*

³ *St. Petersburg Electrotechnical University, 197376 St. Petersburg, Russia*

⁴ *Slovak University of Technology, 81219 Bratislava, Slovak Republic.*

⁵ *National Institute of Standards and Technology, Boulder, Colorado, USA*

(Distribution version of manuscript for submission for publication in Phys. Rev. B, target submission date 9 Feb 2009)

Brillouin light scattering (BLS) has been used to observe and confirm the existence of nonlinear three magnon splitting and confluence processes for propagating spin waves in the magnetostatic backward volume wave (MSBVW) configuration. Wave-vector and frequency selective BLS techniques were also used to provide a quantitative map of the wave vector make-up for the parametrically excited half-frequency dipole-exchange spin wave (DESW) split magnons and the confluence magnons that result from the recombination of these DESW modes. The experimental wave vector maps for the product splitting and confluence magnons matched nicely with those expected from spin-wave theory. The data were obtained with (1) a strip line excitation/detection transducer structure, (2) forward scattering BLS optics, (3) a fixed magnetic field of 352 Oe applied along the propagation direction, (4) pumping frequencies from 2.5 down to 2.1 GHz, (5) and cw input powers from 200 μ W to 6 mW. The wave-vector selective measurements utilized variable diameter circular diaphragms, rotatable slit apertures, and circular light blocks to access spin waves with wave numbers from about 100 to 3.6×10^4 rad/cm and the full 360° range of propagation angles.

PACS numbers: 05.45.-a, 75.30.Ds, 76.50.+g, 78.35.+c, 85.70.Ge

I. INTRODUCTION

During the last several decades, extremely low loss magnetic thin films, and yttrium iron garnet (YIG) films in particular, have been used to study a wide variety of linear and nonlinear spin-wave phenomena at microwave frequencies. In addition to the relevance of these effects to problems in magnetodynamics, the results are also of fundamental importance for the understanding of wave behavior in dispersive dissipative media in general. Currently there are three main areas of interest in the study of nonlinear magnetization dynamics in magnetic films, (i) microwave-driven parametric spin-wave processes, often termed Suhl instabilities,¹⁻³ (ii) modulational instability and stationary spin-wave excitations such as envelope solitons,⁴⁻⁸ and (iii) chaotic nonlinear dynamics.^{9,10} All three of these classes of nonlinear magnetodynamics effects involve nonlinear spin-wave interactions through so-called three or four wave processes.

This paper focuses on item (i), and in particular, three wave splitting and confluence processes and the elucidation of these interactions by wave-vector selective Brillouin light scattering (BLS). In 2000, Synogach *et al.*¹ were the first to demonstrate the role of parametric three wave processes in the creation of ultra short microwave pulses in YIG film spin-wave propagation structures. The data, while convincing, were comprised of microwave results only. In 2003, Mathieu *et al.*² were able to use time and space resolved BLS techniques to obtain direct images of the propagating half-frequency spin waves produced by the three wave splitting interactions. Interestingly, these images revealed very low velocity wedge shaped wave fronts with the parametric spin waves

concentrated along the leading edge. These results had one missing link, namely, no direct evidence for the companion confluence process by which the half-frequency magnons recombine to make the narrow pulse magnons at the initial signal frequency.

This missing link is addressed here. Continuous wave microwaves were used to excite spin waves in a YIG film magnetostatic backward volume wave (MSBVW) propagation structure. Carefully measured BLS spectra for different input power levels revealed both the half-frequency peak that is the signature of the parametric magnons from the three wave splitting as well as a prominent signal that was only slightly downshifted in frequency from the initial pumping frequency. Detailed wave-vector selective BLS measurements served to identify this signal as due to a confluence of the parametric magnons. This represents the first direct observation of three wave confluence processes in magnetic systems. It also represents the first direct observation of splitting for MSBVW spin waves.

Section II describes the basic BLS/microwave experiment as well as operational details on wave vector selective measurements. Section III presents representative BLS data that comprise the experimental evidence for the three wave splitting and confluence processes and makes qualitative connections with the governing dipole exchange spin wave (DESW) frequency-wave number dispersion relations. Section IV presents additional wave-vector selective BLS data that serve to identify the explicit nature of the splitting and confluence magnon products from the pumped MSBVW spin waves. Section V provides brief comments on the effect of small changes in the pumping frequency on the magnon

splitting and confluence processes elucidated in the earlier sections. Section VI provides a summary and conclusions.

II. MICROWAVE AND BRILLOUIN LIGHT SCATTERING SET-UP

The key microwave component of the set-up was the spin-wave propagation structure. This was comprised of a long and narrow YIG film strip in a standard MSBVW spin-wave (SW) delay line configuration.⁷ The strip was 20 mm long, 2 mm wide, and 6.3 μm thick. The low loss YIG film was grown by standard liquid phase epitaxy techniques. The 5 GHz ferromagnetic resonance half power line width was about 0.5 Oe. A pair of 50 μm -wide and 2 mm-long microstrip transducers with a separation of 7 mm was used to excite and detect the propagating spin waves. For propagation in the MSBVW configuration, the static external field H was applied parallel to the long dimension of the strip and the SW propagation direction. The field was set at a nominal value of 352 Oe for all of the measurements. The cw microwave input was at a pumping frequency f_p of 2.5 GHz for most of the measurements. For the frequency effect study in Sec. V, additional f_p -values from 2.4 to 2.1 GHz were also used. For the BLS measurements shown below, the nominal input microwave power level at the launch transducer ranged from about 200 μW to 6 mW. Some of the preliminary microwave measurements were done at powers down to one microwatt or so. These data indicated a Suhl threshold power level in the range of 1 μW or so.

The above field-frequency operating point was chosen subject to two criteria. The first is the realization of a strong SW signal at the output transducer. 2.5 GHz sits at the maximum of the MSBVW amplitude vs. frequency transmission curve for the structure at 352 Oe. This operating point corresponded to a wave number k for the pumped magnons on the lowest order MSBVW dipole exchange spin wave (DESW) of about 100 rad/cm. The second is the need to ensure that three wave splitting processes are allowed. In practical terms, this means that spin waves at $f_p/2$ are supported by the propagation structure.² At $H = 352$ Oe, the bottom of the MSBVW dipole-exchange spin wave band sits at about 1.1 GHz, well below $f_p/2$.

The BLS measurements were performed using a multipass tandem Fabry-Perot interferometer (TFPI) in a forward scattering configuration, with and without wave-vector selectivity. The basic forward scattering approach to the analysis of pumped spin-wave excitations in YIG films was first developed by Srinivasan and co-workers.^{11,12} Wave-vector selective BLS analysis techniques for spin waves were first developed by Wilber and co-workers.¹³⁻¹⁵

The overall measurement approach used here follows Mathieu *et al.*² For the current experiments, a 514.5 nm wavelength linearly polarized argon ion laser light was focused onto the YIG film by a 12 cm focal length lens at normal incidence with 10 mW incident power. The directly transmitted and scattered light was collected by a 50 mm focal length, and 30 mm diameter F1.4 camera lens. A polarizing filter set perpendicular to the incident light polarization was used to reduce substantially the intensity of the directly

transmitted beam. Magnon scattered light generally experiences a 90° rotation in polarization from the incident beam.

The wave-vector selective BLS measurements were done in two ways. First, different sized on-axis circular apertures formed from a variable diaphragm behind the collection lens were used to vary the maximum magnon wave number k_{max} for the forward scattered light. Second, wave vector directions were selected through the use of a 1 mm wide slit-type aperture placed behind the collection lens. The slit orientation relative to the applied field defines the usual polar spin wave propagation angle θ_k .

Figure 1 illustrates the scattering geometry and the wave-vector selection process described above. The figure shows the YIG film propagation structure and the collection optics. The arrows show the incident light with wave vector \mathbf{q}_i and the scattered light at \mathbf{q}_s that results from the interaction with a magnon with wave vector \mathbf{k}_{max} . This upper limit on $|\mathbf{k}_{\text{max}}|$ is defined by the radius of the on-axis diaphragm shown schematically on the far right side of the diagram. The opening limits the scattered light into the spectrometer to those photons that derive from magnons with wave numbers (k) less than some k_{max} . If one uses the 1 mm wide slit instead of the diaphragm, as indicated by the dashed lines, then one can further limit the selected magnon wave vector to a specific propagation angle θ_k . This is strictly true for k -values above 1000 rad/cm or so, well within the bounds of the data considered below. A full slit that extends over the entire aperture of the collection lens, as indicated by the dashed rectangle, was used for the initial scans to determine the θ_k -values for strong scattering. A special slit that extends only in one direction from the optic axis was used for the quantitative wave-vector selective measurements to be considered in Sec. IV.

For the wave-number measurements for the confluence magnons in section IV, an additional wave-vector selection process was used. In this set up, instead of a diaphragm, different size on-axis circular light blocks were used. The diameter of the block plays the same role as the diameter of the diaphragm in Fig. 1, except than one now selects out wave numbers above some k_{min} value instead of k -values below

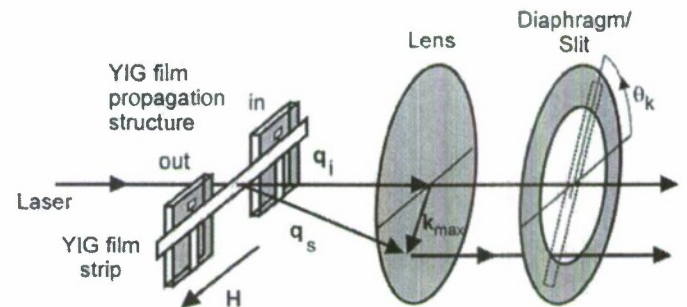


FIG. 1. Schematic diagram of the wave-vector selection scattering geometry. The laser light is incident on the yttrium iron garnet (YIG) film spin wave propagation structure at wave vector \mathbf{q}_i , with a scattered light wave vector \mathbf{q}_s and a magnon wave vector \mathbf{k}_{max} oriented at an angle θ_{max} relative to the direction of the applied field H . The collection lens and the diaphragm/slit assembly define the selected magnon wave vector.

some k_{\max} .

Through the above scheme, one can perform a full range of wave vector selective BLS measurements. Separate data runs for different diameter (d) diaphragms or circular light blocks, for example, can allow one to separate out the scattering associated with specific wave numbers. Diaphragms with d -values from 1 mm to 30 mm were used, typically in increments of 1 or 2 mm. The corresponding k_{\max} values are 1.2×10^3 rad/cm and 3.6×10^4 rad/cm, respectively. Light blocks with d -values from 2 mm to 10 mm were used. These diameters give a range of k_{\min} from 2.4×10^3 to 1.2×10^4 rad/cm. Measurements were always made with the same light intensity and measuring time. Once the wave number has been determined, data obtained with a slit aperture can be used to separate out the product magnons as a function of propagation angle. The wave-vector selectivity capability is crucial to the identification of the product spin waves for the nonlinear three magnon splitting and confluence processes that are the focus of this paper. The data presented in Sec. IV will illustrate the very different wave-vector make-up for the parametrically excited DESW $f_p/2$ magnons from the splitting process and the product spin waves that come from the confluence of these magnons.

III. PARAMETRIC DESW AND CONFLUENCE MAGNONS

How do the BLS data reveal the presence of the relevant magnons? Figure 2 shows representative BLS spectra of scattering intensity vs. frequency for different input cw power levels, as indicated. The frequency axis shows the scattered photon frequency relative to the laser frequency. The frequency axis goes from positive, or anti-Stokes (AS), on the left, to negative, or Stokes (S), on the right. The strong

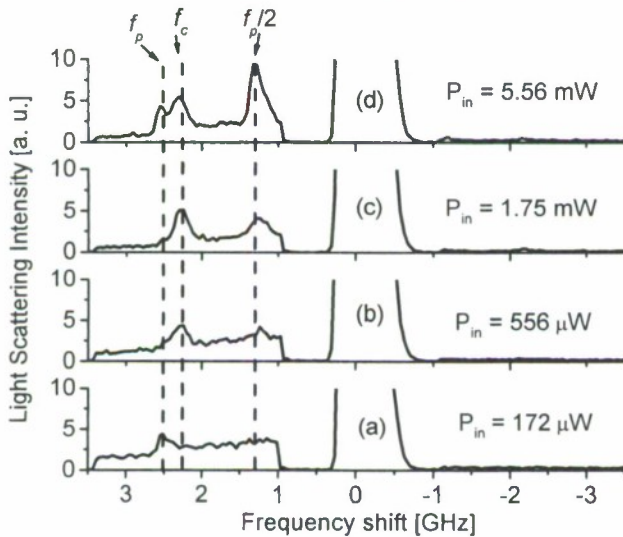


FIG. 2. Representative Brillouin light scattering spectra of scattering intensity vs. frequency for different input microwave cw power levels (P_{in}), as indicated. The pump frequency (f_p) was 2.5 GHz. The static external field was set to 352 Oe. The nominal spectrometer free spectral range was 8 GHz. There were no wave-vector selective diaphragms in place and the measuring time was the same for all scans. The vertical dashed lines and labels identify different peaks in the spectra at f_p , at f_c , slightly below f_p , and at $f_p/2$.

Rayleigh peak at zero frequency comes from the laser line. The incident beam was positioned in the middle of the YIG strip about 2 mm down line from the input transducer. The microwave pumping frequency was 2.5 GHz. The static magnetic field was set at 352 Oe. All measurements were made with the same incident light intensity, the wave vector selective diaphragm removed, and the same TFP scanning parameters.

Note also that the scans in Fig. 2 show magnon signals only on the positive frequency AS side of the spectra. This AS region was scanned at a slow scan rate in order to bring out the magnon structure. Note that this AS region corresponds to scattering in which one of the microwave or parametrically pumped magnon is destroyed and a photon is created. Generally speaking, the BLS peaks for the pumped magnons at f_p and the $f_p/2$ split magnons are found to be stronger on the AS side of the spectra. Intuitively, this is consistent with the nature of the scattering from magnons driven to large occupation numbers by either the microwave pumping process or the subsequent interactions that produce the parametric magnons. For the confluence magnons, however, it turns out that the Stokes as well the Anti-Stokes sides of the spectra are needed to obtain a full picture of the excited modes. Such AS-S confluence magnon effects will be considered in Sec. IV.

The spectra examples in Fig. 2. show three things. (1) There is a peak in the spectra at the pumping frequency that is strong at low power, weakens at intermediate power levels, and then strengthens again at the highest power shown. (2) As the power is increased, one sees an additional peak at $f_p/2 \approx 1.25$ GHz appear and grow in strength. (3) One can also see the appearance and growth of a third peak at $f_c \approx 2.25$ GHz, positioned slightly below the f_p peak in frequency, as the power level is increased.

In reference to item (1), the initial drop and subsequent increase in intensity for the peak in the spectra as the power level is increased is a likely indication of the role of the three magnon processes that are in play here. Microwave data for manganese ferrite (MgF) in the initial Suhl paper on ferromagnetic resonance saturation shows a gradual decrease in the microwave loss as one moves above threshold.³ The data in Ref. 3, however, do not extend to the extreme 25-40 dB above threshold levels needed to match the results in Fig. 2. Moreover, the nature of the MgF samples is not specified. One possible scenario is that, as the power is initially increased well above threshold, more and more of the energy of the pumped magnons is passed to the parametric magnons and the peak at f_p drops in strength. As the power is further increased, these parametric processes level off and the f_p peak grows again.

For item (2), the growth of the $f_p/2$ magnon splitting peak with increasing power provides direct evidence for the scenario above. This is actually a threshold effect similar to that found for Suhl processes. There is a critical power level, typically at the one microwatt level, for the onset of the splitting process. Even so, the splitting signal is not discernable from the BLS data until the input power is much higher, as in the (b) graph of Fig. 2. As elaborated below, these product magnons for the splitting process have a range of frequencies distributed around $f_p/2$. The growth in the peak at f_c [item (3)] slightly below f_p is ascribed to the confluence of some

subset of these split magnons. The concluding discussion for this section, given below, provides qualitative connections between these data and the proposed magnon splitting and confluence processes. Quantitative connections will follow in Sec. IV, based on detailed wave-vector selective measurements.

These connections are based on the schematic MSBVW spin wave dispersion diagrams and specific spin-wave mode points shown in Fig. 3. A detailed description of the nomenclature is given in the expanded figure caption. The curves were computed from the standard DESW theory in Ref. 16, standard YIG parameters, and the same film thickness and static field cited for the measurements. The identified mode points are intended to make qualitative connections with the BLS results.

Note that the actual parametric modes need not have wave vectors that are strictly co-linear with the field. Keep in mind that a given MSBVW pumped magnon at f_p and wave vector \mathbf{k}_p will split into two parametric magnons with frequencies f_{s1} and f_{s2} and wave vectors \mathbf{k}_{s1} and \mathbf{k}_{s2} , respectively. Energy and momentum conservation impose the conditions $f_p = f_{s1} + f_{s2}$ and $\mathbf{k}_p = \mathbf{k}_{s1} + \mathbf{k}_{s2}$. Since $|\mathbf{k}_p|$ is very small compared to $|\mathbf{k}_{s1}|$ and $|\mathbf{k}_{s2}|$, it is clear that \mathbf{k}_{s1} and \mathbf{k}_{s2} must be nearly equal and oppositely directed. The dispersion curve constraints also force both \mathbf{k}_{s1} and \mathbf{k}_{s2} to be nearly co-linear with the field. Similar remarks apply to the reverse confluence process that take various pairs of split magnons into modes at frequencies close to f_c . The up shift in frequency to $f_k \approx f_c$ in this case leads to allowed modes at relatively large propagation angles. As the data of the next section will show, the parametric spin waves turn out to have in-plane propagation angles away from the field direction by $\pm 10^\circ$ or so for the split $f_p/2$ magnons and by $\pm 45^\circ$ or so for the confluence f_c magnons.

Overall, Fig. 3 shows a consistent map of the connections between the initially excited cw MSBVW spin wave signal in the YIG strip and the parametric magnons observed from the BLS measurements. If one considers a low wave-number MSBVW mode at f_p (upper open diamond), magnon splitting processes that conserve frequency and momentum give product magnons as indicated by the square and circle points clustered around the $f_p/2$ line cut in the figure. At the same time, the lower frequency subset of these split magnons can be combined to give a confluence peak at f_c . The dashed box in the lower central part of Fig. 3 identifies two such modes.

The layout of modes in Fig. 3 leads to one more important connection with the data. Note that both the splitting peak in Fig. 2 at $f_p/2$ and the confluence peak at f_c are rather broad. Based on the scenario given above, one can explain the $f_p/2$ line broadening in terms of the relatively wide band of split magnons shown by the circle and square points in Fig. 3. It also stands to reason that if the observed split magnon peak is broad, any peak due to the confluence of these magnons will also be broad.

Taken at face value, the connections implied in Fig. 3 are nothing more than conjecture. The mode connections are based entirely on the dispersion curves shown and the frequencies match those found in the experiment. What remains is to show, from actual wave-vector selective BLS data, that the split modes clustered around $f_p/2$ in frequency and the product low

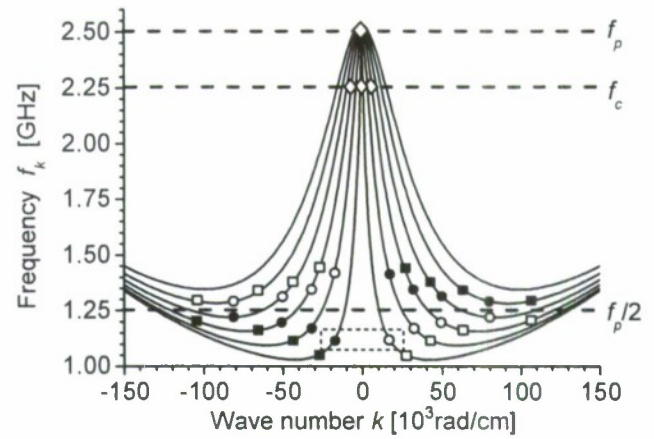


FIG. 3. Schematic dispersion curves of spin wave frequency f_k vs. wave number k with mode connections. The curves are for the first six dipole-exchange spin wave branches for in-plane propagation parallel or anti-parallel to the field H and an H -value of 352 Oe, the same as for the data in Fig. 2. The horizontal dashed lines label the frequencies for the three peaks identified in Fig. 2 for the directly pumped magnetostatic backward volume wave (MSBVW) spin waves at $f_p = 2.5$ GHz, confluence magnons at f_c , and splitting magnons at $f_p/2$. The open diamond at f_p labels the MSBVW operating point. The matching pairs of solid and open circles and squares show, in schematic form, parametrically excited split magnons at $\pm k$ and with f_k values equally shifted up and down from the $f_p/2$ line. The open diamonds for a range of low $|k|$ values on the f_c line show the nominal position in frequency and wave number for the confluence magnons. The dashed square close to 1.12 GHz identifies split magnons that give a confluence magnon at f_c .

wave-number confluence modes at f_c match the data.

IV. WAVE VECTOR SELECTIVE ANALYSIS

The techniques and procedures for the wave-vector selective BLS analysis were outlined in Sec. II. Recall that there are two stages in the analysis for the split magnons, one with a variable diameter diaphragm for wave-number analysis and one with a rotating slit aperture for wave-vector direction analysis. Recall the key feature of the stage one measurements, namely, the clear and distinct $f_p/2$ peak in Fig. 2(d) that appears suddenly when the diameter of the wave-vector selective aperture is larger than about 9 mm. This critical d -value corresponds to $k_{\max} \approx 1.1 \times 10^4$ rad/cm. This is precisely the minimum allowed k -value for $f_p/2$ magnons from DESW theory. This match-up comprises prima facie evidence for the connection with DESW magnons as proposed above.

Figure 4 shows representative wave-vector selective BLS data for the $f_p/2$ peak in Fig. 2 and companion iso-frequency magnon wave-vector contour plots for the low order DESW spin-wave dispersion branches at $f_k = f_p/2$. Graph (a) shows the BLS signal as a function of the cut-off k_{\max} wave number value. The vertical dashed lines denote the upper and lower limit k_{\max} values for the diaphragm set-up described above. Figure 4(b) shows calculated iso-frequency contour plots for the 1.25 GHz cut of the dipole-exchange spin wave dispersion surface. While the horizontal axes for both graphs correspond

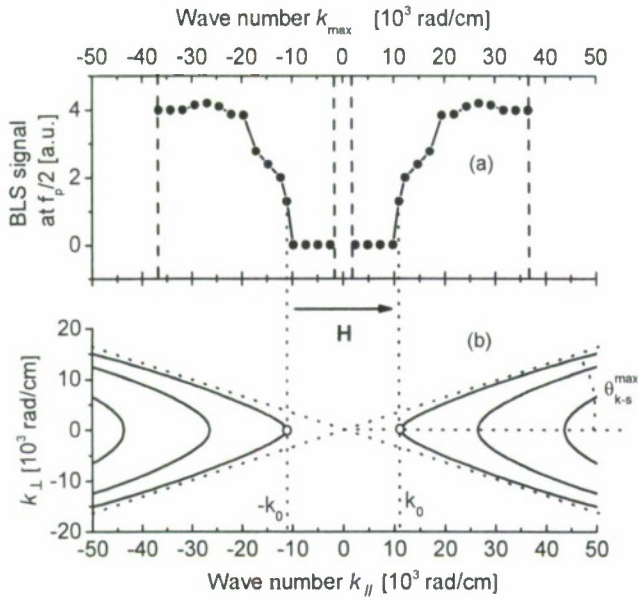


FIG. 4. (a) BLS scattering signal at $f_p/2$ as a function of the maximum allowed wave number k_{\max} for an input power of 5.56 mW and $f_p = 2.5$ GHz. The vertical dashed lines denote the limit k_{\max} values for the experimental diaphragm set-up. (b) Theoretical iso-frequency contour plots of the transverse in-plane spin wave wave-vector component k_{\perp} vs. the parallel component k_{\parallel} for the four lowest order DESW modes at $f_p/2$. The plot was obtained from the DESW theory of Ref 16, with parameters that match the experiment. The open circles and k_0 labels mark the low limit for the available DESW spin waves at $f_p/2$. The angle θ_{k-s}^{\max} labeled in (b) shows the maximum allowed spin wave propagation angle.

to wave number, the plotted parameter in (b) corresponds to the component of the in-plane DESW wave vector \mathbf{k} that is parallel to the static field \mathbf{H} , labeled as k_{\parallel} . For comparison purposes, the horizontal scales for (a) and (b) are the same. The vertical scale in (b) corresponds to the in-plane transverse component of \mathbf{k} , labeled as k_{\perp} . For reference purposes for the discussion of the angle data to follow, the θ_{k-s}^{\max} labeled in (b) indicates the maximum theoretical in-plane spin-wave propagation angle for the half-frequency spin waves.

The data in (a) and the iso-frequency contours in (b) confirm the match-up noted in the introduction to this section. The onset of detected spin waves as a function of the experimental k_{\max} value occurs precisely at the theoretical lower limit k value at $k_0 \approx 1.1 \times 10^4$ rad/cm for the half-frequency DESW spin waves. These lower limit k -values are marked in (b) by open circles. Note that this onset point in (b) is for a DESW propagation direction that is parallel to the static field and with a propagation angle θ_k equal to zero or 180° only. The full iso-frequency contours in (b), however, provide much more information that the confirmation of this onset point for split magnons. The contours allow one to read off the allowed propagation angles for the split magnons with $k > k_0 = 1.1 \times 10^4$ rad/cm. From these plots, one expects that the angle selective BLS data will reveal spin-wave propagation angles for the half-frequency spin waves in the range $-\theta_{k-s}^{\max} < \theta_k < \theta_{k-s}^{\max}$ and $(180^\circ - \theta_{k-s}^{\max}) < \theta_k < (180^\circ + \theta_{k-s}^{\max})$.

As noted previously, θ_k resolved BLS data were obtained with a rotating slit-type aperture scheme. In order to resolve

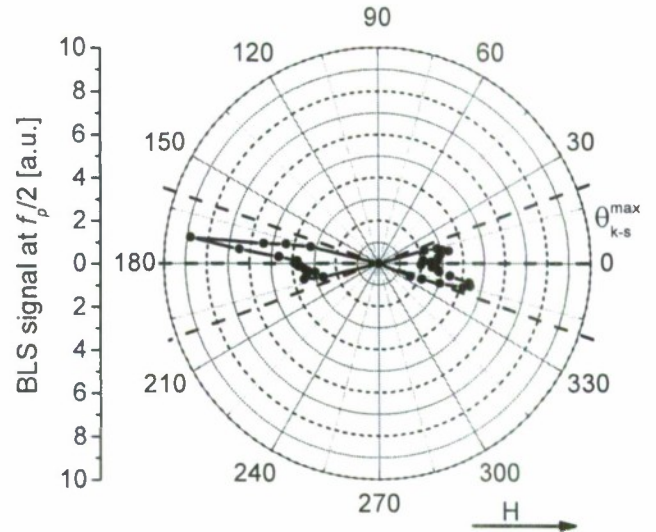


FIG. 5. Polar representation of the BLS signal for the $f_p/2$ DESW magnon peak as a function of the slit aperture rotation angle θ_k . The arrow shows the direction of the static field \mathbf{H} . The dashed lines denote the double sector of spin wave propagation angles for $-\theta_{k-s}^{\max} < \theta_k < \theta_{k-s}^{\max}$ and $(180^\circ - \theta_{k-s}^{\max}) < \theta_k < (180^\circ + \theta_{k-s}^{\max})$ that match the range of allowed θ_k values from Fig 4b.

the full $0-360^\circ$ range of possible θ_k -values, the measurements were done with a half slit arrangement that extends outward from the optical axis in one direction only, rather than the full slit shown in Fig. 1. Figure 5 shows a representative polar plot of BLS intensity data as a function of θ_k for the $f_p/2$ split magnon peak in Fig. 2(d) at $P_{\text{in}} = 5.56$ mW. As in Fig. 4, the field is parallel to the $\theta_k = 0$ direction. The data were obtained for angular steps of 2° and with the same scanning times for all measurements. The dashed lines at angles of θ_{k-s}^{\max} to the horizontal mark the expected range of pumped magnons from Fig. 4. The angular distribution of the DESW $f_p/2$ magnons is clear from the figure and no extensive discussion is needed here. The data show, rather unambiguously, that the BLS signal is constrained within a double sector of angles within $\pm\theta_{k-s}^{\max}$ of the field axis. The span of observed propagation angles matches nicely to the contour plot in Fig 4(b).

The above data and theoretical connections provide a complete map of the DESW $f_p/2$ magnons that result from the three wave splitting process for pumped MSBVW magnons. Both the directly measured wave numbers and the propagation directions of the split magnons match nicely to theory. This represents the first direct experimental map of three magnon splitting processes in any magnetic system pumped in the backward wave configuration.

Turn now to the confluence magnons. Recall that in this case, blocking circles as well as diaphragms and slit apertures were used for the wave-vector selective measurements. The changes in intensity with diaphragm diameter d for the f_c peak are quite different from those for the split magnons. In this case, the signal increases steadily as d is increased from 1 to 6 mm and then appears to increase at a slightly lower rate up to the limit d -value of 10 mm. This implies that the predominant confluence magnon k -values are generally below

about 10^4 rad/cm or so. For the light block in place of the diaphragm, the f_c peak signal intensity starts high and gradually diminishes to near zero as d is increased from the initial 2 mm value to the 10 mm upper limit value. This serves to confirm a confluence magnon distribution with $k < 10^4$ rad/cm and predominant k -values somewhat below this limit. At the same time, the slit aperture data indicate propagation angles that are typically 30° - 60° and 120° - 150° away from the field axis. Recall that the split magnons are all very close to the field axis. It is clear from these results that the wave vector make-up of the confluence magnons is very different from that for the split magnons.

Figure 6 shows representative wave-vector selective BLS data for the f_c peak in Fig. 2 and companion iso-frequency magnon wave vector contour plots for the low order DESW spin-wave dispersion branches at $f_k = f_c$. Graph (a) shows the f_c peak intensity as a function of the diaphragm and light block cut-off wave numbers, k_{\max} and k_{\min} , as indicated. The shaded curve at the bottom of the graph provides a qualitative indication of the f_c magnon k -distribution implied by the two sets of data. Graph (b) shows calculated iso-frequency contour plots for the 2.25 GHz f_c cut of the dipole-exchange spin-wave dispersion surface. The angle θ_{k-c}^{\max} indicates the maximum theoretical in-plane spin wave propagation angle for the confluence magnons. Graph (c) shows representative BLS data in a polar plot representation for the f_c confluence magnon peak in Fig. 2. In order to obtain the somewhat balanced 4-lobe plots shown in (c), it was necessary to use both anti-Stokes positive frequency side BLS data for $90^\circ < \theta_k < 270^\circ$ and Stokes negative frequency side data for $-90^\circ (270^\circ) < \theta_k < 90^\circ$.

The results in Fig. 6 provide a useful map of the magnon make-up for the BLS confluence peak. These results also demonstrate the marked difference between these confluence magnons at f_c and the split magnons at $f_p/2$ discussed at the start of this section. Graph (a), for example, shows that the f_c magnons are limited to k values below 10^4 rad/cm, while the

data in Fig. 4 show that the split magnons are all at wave numbers well in excess of 10^4 rad/cm. Graph (b) shows, moreover, that the expected angular distribution of the f_c magnons emphasizes propagation directions at about 45° or so, relative to the field axis, while the predominant θ_k values for the split magnons are much closer to the field axis. The angular data in (c) confirm that the magnons associated with the f_c peak do, in fact, give polar plot lobes that match the theory.

V. PUMPING FREQUENCY DEPENDENCES

The results in Secs. III and IV serve to quantify the presence of (1) DESW $f_p/2$ magnons that result from the parametric three wave splitting process for pumped MSBVW magnons, and (2) confluence magnons at f_c that result from the recombination of the DESW magnons. The wave-number make-up and propagation characteristics of these magnons were mapped experimentally and connected to theory. All of these results, however, are based on data for one fixed value of the in-plane field and one specific drive frequency selected for strong coupling to the pumped MSBVW mode. This section is concerned with one further test of the mode connections established above, based on the effect of changes in the pumping frequency f_p on the BLS response, with the field held at the same value as before. The strategy here is similar to that of Synogach *et al.* in Ref. 1. In that work, done for the case of pumped magnetostatic surface modes, an increase in both the field and the pumping frequency resulted in an upward shift in both the spin wave band and the operating point frequency to the point where three magnon splitting processes are no longer allowed. This elimination of three magnon splitting processes resulted in a major change in the microwave response of the surface wave delay line structure.

The approach here is much simpler. The field was held at the same value as before, but now, the pumping frequency was gradually decreased to the point where the downshifted $f_p/2$ cut across the spin wave dispersion curve diagram falls below

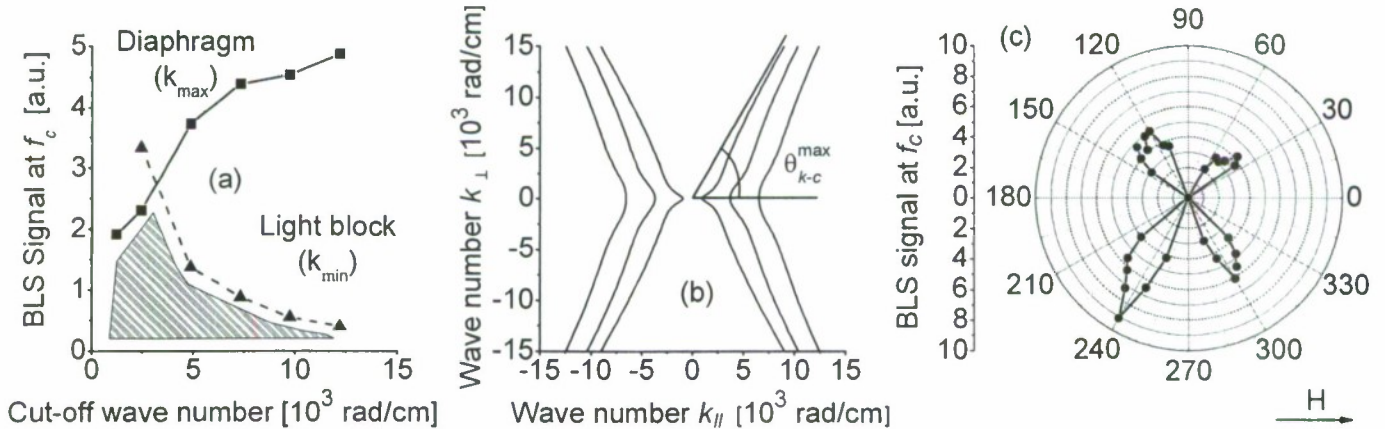


FIG. 6. (a) Data on the BLS scattering signal level at the f_c peak vs. the two limit wave numbers k_{\min} and k_{\max} , as obtained for different diameter light blocks or diaphragms, respectively. The dashed light gray area gives a qualitative estimate of the confluence magnon k -distribution implied by these data. (b) Theoretical iso-frequency contour plots of the transverse in-plane spin wave wave-vector component k_{\perp} vs. the parallel component k_{\parallel} , as referenced to the field direction, for the five lowest order DESW modes at f_c . The plot was obtained from the DESW theory of Ref 16, with parameters that match the experiment. The angle θ_{k-c}^{\max} corresponds to the maximum allowed spin-wave propagation angle for confluence magnons at the f_c frequency cut. (c) Polar representation of the BLS signal level at the f_c peak as a function of the slit aperture rotation angle for the input power of 5.56 mW. The arrow shows the direction of the static magnetic bias field H .

the bottom of the band of DESW modes. One can see this basic effect from Fig. 3. The bottom of the band sits at about 1.0125 GHz. This means that a pumping frequency below about twice this value, or 2.025 GHz, will be low enough to eliminate the possibility of any three magnon splitting response at all. One can also see that as the pumping frequency is gradually lowered, the $f_p/2$ cut of modes across the bottom of the band will become narrower and narrower and the mean k -value for the split magnons will shift out to about 4×10^4 rad/cm just before the splitting response vanishes. This will also cause the f_c point for the confluence magnons to move closer and closer to f_p .

Panels (a) - (d) in Fig. 7 show the effect of a lowering of the pump frequency on the spectra in Fig. 2. The data go from the range where three magnon splitting is readily allowed, as in (a) for $f_p = 2.4$ GHz, to a range where such processes are barely allowed, as in (d) for $f_p = 2.1$ GHz. All data were obtained for the same configuration and parameters as for the data in Fig. 2(d), except for the shift in pumping frequency. The three vertical dashed lines in (a) and (b) mark the pumping frequency operating point (f_p), the confluence (f_c) and splitting ($f_p/2$) peaks from the data, as indicated. In (c), the two vertical dashed lines mark the f_p and $f_p/2$ points only. In this case, the f_c point is so close to the operating point that the two frequencies are indistinguishable. The single vertical dashed line in (d) marks the f_p point only. The arbitrary unit [a.u.] vertical axis BLS intensity scales for the four graphs show self consistent relative values. The matching scales for

(a), (b), and (c) demonstrate the evolution of the spectra and the individual intensities with the drop in frequency. The larger range for (d) shows the rapid rise in the strength of the f_p peak as one approaches the cut-off point for splitting.

The four panels in Fig. 7 demonstrate the evolution scenario outlined above. Recall that as f_p is gradually reduced, the gap between the $f_p/2$ and the bottom of the band becomes smaller and smaller. This means that the f_c point must also move closer and closer to f_p . This is precisely what one sees from panels (a) - (c) in Fig. 7. For (a) the f_p to f_c spacing has dropped from the nominal 0.25 GHz value in Fig. 2 to 0.1 GHz. For (b) this spacing has dropped further to about 0.05 GHz. In (c), the f_c peak position is not even discernable from f_p on the scale of the graph. Finally, for the case shown in Fig. 7(d), with the bottom of the band at about 1.02 GHz and $f_p/2$ at 1.05 GHz, the half frequency point is so close to the bottom of the band that the splitting and confluence effects of interest here no longer occur. In panel (d), one sees that the $f_p/2$ splitting peak has disappeared entirely and the peak at f_p has increased in intensity by a factor of 3 or so.

The above points mainly relate to the evolution in the shape of the spectra as the pumping frequency is decreased. Note also that the data show a clear degradation in the shape of the $f_p/2$ splitting peak as one goes from panel (a) to panel (c). This degradation can be attributed, quite plausibly, to two things, (1) the move of the $f_p/2$ frequency cut closer and closer to the bottom of the band, and (2) the wave number limits in the collection optics. From Fig. 3, one can see that as one moves from the situation shown to a pump frequency at the bottom of the band, the k -values for the split frequency modes that contribute to the confluence will move from the indicated value of about 2×10^4 rad/cm out to about 4×10^4 rad/cm. At the same time, the maximum k -value that can be accessed by the collection lens is about 3.6×10^4 rad/cm. This means that the somewhat washed out $f_p/2$ peaks in (b) and (c) are for wave numbers that approach or exceed the limits of the set-up.

V. SUMMARY AND CONCLUSION

Three magnon splitting and confluence processes in thin YIG films for the MSBVW propagation configuration has been experimentally observed by Brillouin light scattering measurements and confirmed by wave-vector selective analysis. A complete characterization for both of these nonlinear processes has been made. The change in the response with pumping frequency as well as the fully analyzed wave-vector make up of the product magnons provide proof positive of these processes. Interestingly, and perhaps fortuitously, the data reveal a confluence response for only selected half-frequency split magnons that are slightly downshifted from the strict half-frequency point. This state of affairs pushes the confluence peak to a point slightly below the peak at the signal frequency and renders it observable.

ACKNOWLEDGMENTS

This work was supported in part by the United States Army Research Office, MURI, Grant W911NF-04-1-0247, the

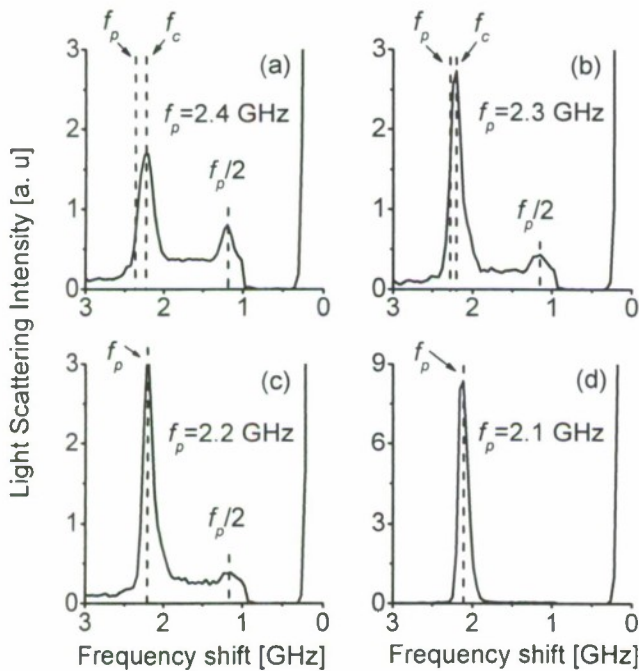


FIG. 7. Representative BLS spectra of scattering intensity vs. frequency for different pumping frequencies. (a) $f_p = 2.4$ GHz, (b) $f_p = 2.3$ GHz, (c) $f_p = 2.2$ GHz and (d) $f_p = 2.1$ GHz. The static external field was set to 352 Oe. The nominal spectrometer free spectral range was 8 GHz. There were no wave-vector selective diaphragms or light blocks in place and the measuring time was the same for all scans. The vertical dashed lines and labels identify different peaks in the spectra at f_p , at f_c , and at $f_p/2$.

United States Office of Naval Research, Grants N00014-07-1-0597 and N00014-08-1-1050 (through sub-award PT103701-SC101157 from Virginia Commonwealth University), and the Russian Foundation for Basic Research, grant 08-02-00959. Dr.

Ward L. Johnson, National Institute of Standards and Technology, Boulder, Colorado, is acknowledged for a perceptive reading of the manuscript.

-
- ¹ V. T. Synogach, Yuri K. Fetisov, C. Mathieu and C. E. Patton, *Phys. Rev. Lett.* **85**, 2184 (2000).
 - ² C. Mathieu, V. T. Synogach, and C. E. Patton, *Phys. Rev. B* **67**, 104402 (2003).
 - ³ H. Suhl, *J. Phys. Chem. Solids* **1**, 209 (1957)
 - ⁴ J. W. Boyle, S. A. Nikitov, A. D. Boardman, J. G. Booth, and K. Booth, *Phys. Rev. B* **53**, 12173 (1996).
 - ⁵ M. Bauer, C. Mathieu, S. O. Demokritov, B. Hillebrands, P. A. Kolodin, S. Sure, H. Dötsch, V. Grimalsky, Yu. Rapoport, A. N. Slavin, *Phys. Rev. B* **56**, 8483 (1997).
 - ⁶ H. Xia, P. Kabos, H. Y. Zhang, P. A. Kolodin, and C. E. Patton, *Phys. Rev. Lett.* **81**, 449 (1998).
 - ⁷ O. Büttner, M. Bauer, A. Rueff, S. O. Demokritov, B. Hillebrands, A. N. Slavin, M. P. Kostylev, and B. A. Kalinikos, *Ultrasonics* **38**, 443 (2000).
 - ⁸ N. G. Kovshikov, B. A. Kalinikos, C. E. Patton, E. S. Wright and J. M. Nash, *Phys. Rev. B* **54**, 15210 (1996)
 - ⁹ V. E. Demidov and N. G. Kovshikov, *Tech. Phys. Lett.* **24**, 274, (1998); *Tech. Phys. Lett.* **24**, 647, (1998).
 - ¹⁰ M. Wu, B. A. Kalinikos, and C. E. Patton, *Phys. Rev. Lett.* **95**, 237202, (2005)
 - ¹¹ G. Srinivasan and C. E. Patton, *IEEE Trans on Magnetics*, **5**, 1797 (1985)
 - ¹² G. Srinivasan, C. E. Patton, and P. R. Emtage, *J. Appl. Phys.* **61**, 2318 (1987).
 - ¹³ W. Wettling, W. D. Wilber, P. Kabos, and C. E. Patton, *Phys. Rev. Lett.* **51**, 1680 (1983).
 - ¹⁴ W. D. Wilber, W. Wettling, P. Kabos, and C. E. Patton, and W. Jantz, *J. Appl. Phys.* **55**, 2533 (1984).
 - ¹⁵ W. D. Wilber, J. G. Booth, C. E. Patton, G. Srinivasan, and R. W. Cross, *J. Appl. Phys.* **64**, 5477 (1988).
 - ¹⁶ B.A. Kalinikos, *Sov. Phys. J.* **24**, 718 (1981).